Analysis of flux reduction behaviors of PRO hollow fiber membranes: Experiments, mechanisms, and implications

Jun Ying Xiong, Zhen Lei Cheng, Chun Feng Wan, Si Cong Chen, Tai-Shung Chung

www.elsevier.com/locate/memsci

PII: S0376-7388(16)30013-8
DOI: http://dx.doi.org/10.1016/j.memsci.2016.01.012
Reference: MEMSCI14221

To appear in: *Journal of Membrane Science*

Received date: 26 November 2015
Revised date: 5 January 2016
Accepted date: 6 January 2016

Cite this article as: Jun Ying Xiong, Zhen Lei Cheng, Chun Feng Wan, Si Cong Chen and Tai-Shung Chung, Analysis of flux reduction behaviors of PRO hollow fiber membranes: Experiments, mechanisms, and implications, *Journal of Membrane Science,* http://dx.doi.org/10.1016/j.memsci.2016.01.012

Analysis of Flux Reduction Behaviors of PRO Hollow Fiber Membranes: Experiments, Mechanisms, and Implications

Jun Ying Xiong [a], Zhen Lei Cheng [a,1], Chun Feng Wan [a,1],

Si Cong Chen [a], Tai-Shung Chung [a,b,*]

[a] Department of Chemical and Biomolecular Engineering, National University of Singapore, 4 Engineering Drive 4, Singapore 117585, Singapore

[b] Water Desalination & Reuse (WDR) Center, King Abdullah University of Science and Technology, Thuwal 23955-6900, Saudi Arabia

* Corresponding author: Tel.: +65 6516 6645, Email: chencts@nus.edu.sg

[1] These authors contributed equally to this study.

Abstract

Pressure retarded osmosis (PRO) is a promising technology to harvest renewable osmotic energy using a semipermeable membrane. However, a significant flux reduction has been always observed that severely shrinks the harvestable power to a level only marginally higher or even lower than the economically feasible value. This work focuses on the elucidation of various underlying mechanisms responsible for the flux reduction. First, both inner-selective and outer-selective thin film composite (TFC) hollow fiber membranes are employed to examine how the fundamental *internal* factors (such as the surface salinity of the selective layer at the feed side ($C_{F,m}$) and its components) interact with one another under the fixed bulk salinity gradient, resulting in various behaviours of *external* performance indexes such as water flux, reverse salt flux, and power density. Then, the research is extended to investigate the effects of the growing bulk feed salinity due to the accumulated reverse salt flux along PRO modules. Finally, the insights obtained from the prior two stationary conditions are combined with the advanced nucleation theory to elucidate the dynamic scaling process by visualizing how the multiple fundamental factors (such as local supersaturation, nucleation rate and nuclei size) evolve and interplay with one another in various membrane regimes during the whole scaling process. To our best knowledge, it is the first time that the advanced nucleation theory is applied to study the PRO scaling kinetics in order to provide subtle and clear pictures of the events occurring inside the membrane. This study may provide useful insights to design more suitable TFC hollow fiber membranes and to operate them with enhanced water flux so that the PRO process may become more promising in the near future.

Keywords:

Pressure retarded osmosis (PRO); Flux reduction behaviour; Outer-selective hollow fiber membrane; Inner-selective hollow fiber membrane, Gypsum scaling

1. Introduction

Osmotic energy has received growing attention worldwide as an alternative energy. Pressure retarded osmosis (PRO) is a process able to harvest salinity gradient energy by employing a semipermeable membrane between a low salinity feed solution (referred to as "the feed" thereafter) and a high salinity draw solution [1-7]. Comparing to many fossil fuel based energy sources, PRO is a green and sustainable technology friendly to environments because no greenhouse gas and chemicals are released during the harvest of osmotic power.

In spite of the aforementioned advantages over other traditional energy sources, harvesting osmotic energy from PRO processes is still in an infant stage because power density and water flux are severely reduced by many limiting factors, such as internal concentration polarization (ICP), external concentration polarization (ECP), reverse salt permeation, and membrane fouling [7-15]. Even though many breakthroughs have been achieved in recent years on PRO membranes with impressive mechanical strength and power density [7, 8, 14, 16-23], membrane performance deteriorates sharply in real applications [8, 15]. As a result, the net energy drops to a level only marginally higher or even lower than the economically feasible value. Therefore, it is of great importance to investigate the underlying mechanisms responsible for the significant water flux reduction in order to overcome the limitations and design innovative PRO membranes for real practices.

In general, ICP coupled with undesirable reverse salt flux accounts for the water flux decline in PRO processes when the feed pair contains negligible fouling tendency [9, 14, 16, 24]. Prior works have indicated a direct link between intrinsic membrane properties such as water

permeability (A), reverse salt permeability (B), structural parameter (S) and operation conditions (for example, operation pressure ΔP) and external performance indexes such as water flux (J_w), reverse salt flux (J_s), and power density. Yip et al used flat sheet membranes and studied the combined effects of A and B with a relatively small structural parameter [16]. It was found that membranes with a high A value and a moderate B value are highly favourable to achieve outstanding PRO performance, while membranes with a high A value but a very low selectivity (i.e., high B value as well) would suffer from a severe reverse salt leakage, leading to a significantly reduced water flux and projected peak power density at high operation pressures. Zhang and Chung studied the instant and accumulative effects of reverse salt permeation on water flux and power density using 1M NaCl and DI water as the feed pair [14]. Three types of inner-selective thin-film composite (TFC) hollow fiber membranes with different combinations of A, B and S values were used. It was found that a low B value is crucial to suppress the severe flux decline in order to harvest a high power density, while a high B value not only causes an instant drop of water flux but also leads to a significant salt build-up in the feed, resulting in a further rapid flux decline along membrane modules. Sivertsen et al developed a unique iso-watt diagram to link A, B, and S directly with peak power density, enabling an efficient way to compare different membranes [24]. She et al employed HTI CTA flat sheet membranes and specific reverse solute flux (i.e., J_s/J_w, the ratio of reverse salt flux J_s to volumetric water flux J_w) to investigate the effects of various operation parameters in PRO [9]. They found that the significantly reduced water flux was mainly caused by the enhanced ICP due to the severe reverse salt permeation. To date, although most prior works have observed direct links among the intrinsic membrane properties, operation conditions and external performance, the work to systematically elaborate the complicated interactions among them is still absent. By choosing two TFC hollow fiber membranes recently developed in our group, an inner-selective TFC membrane

[8] and an outer-selective TFC membrane [25] (Fig. 1), this work aims to in-depth bridge the intrinsic membrane properties, operation conditions and external performance by elucidating the interactions among some *internal* factors and illustrating their effects on the *external* performance. The internal factors include the surface salinity of the selective layer at the feed side ($C_{F,m}$) and its ICP contribution and J_s contribution, while the external performance comprises water flux (J_w), reverse salt flux (J_s), and power density.

Besides ICP and reverse salt permeation, scaling is another limiting factor responsible for the flux reduction when the feed pair contains scaling precursors [8, 11, 12, 15]. For example, scaling precursors such as Ca^{2+}, $SO_4^{2-}$and HPO_4^{2-} are commonly present in wastewater retentate from wastewater reclamation plants [8, 11, 15]. Zhang et al observed that gypsum precursors such as Ca^{2+} and SO_4^{2-} can cause pore clogging inside the membrane porous support due to the severe ICP of the precursors [11]. They pointed out that the initial rapid flux reduction was due to the significant ICP at high water fluxes, while the subsequent slower flux decline was attributed to the weakened ICP at lower fluxes. They also observed a limiting flux phenomenon similar to the flux behaviors in RO and nanofiltration (NF) processes [26, 27]. To date, although prior works have found that scaling may result in a drastic flux reduction [8, 11, 12, 15], the relationship between pore clogging and flux reduction phenomena still remains unclear. This work aims to elaborate this relationship by employing the advanced nucleation theory, simulation, and experimental studies.

To investigate the underlying mechanisms responsible for the flux reduction, both the inner- and outer-selective TFC hollow fiber membranes will be firstly employed to examine the interactions among the internal factors and their effects on the external performance of PRO

processes. Then the outer-selective TFC hollow fiber membrane will be used in the gypsum scaling study to elucidate the scaling kinetics, especially the relationship between the pore blocking and the flux reduction behaviour. Finally, implications of this study will be discussed to provide useful insights to design more suitable TFC hollow fiber membranes with enhanced water flux so that PRO process may become more promising in the future.

[Fig. 1]

2. Experimental Section

2.1 Materials

Materials used for hollow fiber spinning such as Polyethersulfone (PES), N-methyl-2-pyrrolidone (NMP) et al. were the same as some prior works [14, 20, 25]. Materials for the formation of TFC selective layers such as 1,3,5- benzenetricarboxylic acid chloride (TMC), M-phenylenediamine (MPD), hexane and sodium dodecyl sulfate (SDS) can be found in some prior works [8, 25]. Sodium sulfate (Na_2SO_4, >99% from Sigma-Aldrich) and calcium chloride ($CaCl_2$, 98% from Sigma-Aldrich) were employed as precursors for the gypsum scaling study. Sodium chloride (NaCl, ≥ 99.5% from Merk) was used as the solute for all PRO experiments.

2.2 Fabrication of TFC membranes

The detailed description of PES hollow fiber fabrication has been reported elsewhere [14, 20, 25]. The thin polyamide layers of the inner- and outer-selective TFC hollow fiber membranes were formed via interfacial polymerization [8, 25]. The PES hollow fiber substrate was firstly wetted by a 2%wt MPD aqueous solution for 3-5 minutes. After removing the excess aqueous

solution, an organic hexane phase containing 0.15%wt TMC was introduced to contact with the MPD wetted surface to initiate the cross-linking reaction. After the removal of the residual TMC solution by air purging, the hollow fiber membrane modules were kept in ambient conditions for 2.5 hours before soaking in DI water for experiment studies.

2.3 Characterizations of pure water permeability, salt permeability of TFC hollow fiber membranes

The water permeability (A), salt rejection (R_s), and salt permeability (B) of TFC hollow fiber membranes were determined by testing membranes under the RO mode. The pure water permeability was determined as:

$$A = \left[\frac{\Delta V}{\Delta t}\right] / (A_m \Delta P) \quad (1)$$

where ΔV is the permeate volume collected over a period of time (Δt), A_m is the effective membrane area, and ΔP is the transmembrane pressure. The salt rejection (R_s) was tested under a transmembrane pressure of 1 bar using a 1000ppm NaCl feed solution with salt concentrations measured by a conductivity meter (Schott Instrument Gmbh, Germany). The salt rejection R_s can be calculated as follows:

$$R_s = \left(1 - \frac{C_p}{C_f}\right) \times 100\% \quad (2)$$

in which C_p and C_f are the salt concentrations of the permeate and the feed, respectively. The salt permeability (B) was calculated as follows [28, 29]:

$$B = \frac{1-Rs}{Rs} . A . (\Delta P - \Delta \pi) \quad (3)$$

where $\Delta\pi$ is the osmotic pressure difference across the membrane and ΔP is the transmembrane pressure.

2.4 Determination of TFC hollow fiber membrane performance via PRO tests

The set up for PRO tests has been described elsewhere [20]. The draw solution was introduced to the selective layer side of the module using a high pressure pump (Hydro-cell® from Wanner Engineering , Inc.) at a series of operation pressures, while the feed was recirculated in the other side of the module using a variable-speed gear pump (Masterflex® from Cole-Parmer, Vernon Hill, IL). All PRO tests were conducted in a counter-current flow mode. A constant temperature of the draw solution was maintained at 25±1°C. The weight of the recirculated feed was recorded by a digital data logging software (WinCT-weight).

2.5 Protocols of gypsum scaling tests

To date, most prior scaling studies of TFC hollow fiber membranes have focused on inner-selective membranes [15]. Therefore, gypsum scaling tests in this work were performed using modules made from the outer-selective hollow fiber membrane. For each scaling experiment, the membrane module was first stabilized using 3M NaCl and DI water as the feed pair at 10bar for 30 min. 3M NaCl was chosen to speed up the scaling test; otherwise, it would take a long time to carry out each test and the dilution effect of the draw solution could not be neglected. Then 1M stock solutions containing scaling precursors (Ca^{2+} and SO_4^{2-}) were added into the circulated feed step by step. Firstly, the aqueous sodium sulfate stock solution with a calculated volume was added into the feed (i.e., DI water) drop by drop with mixing. After that the aqueous stock solution containing another precursor (i.e., $CaCl_2$) was sprayed as fine droplets into the feed with mixing to promote a homogeneous distribution of the precursor in the feed. Then the feed solution was pumped to the lumen side of the membrane modules to initiate scaling tests for another 2 hours. Compositions of various feed solutions are listed in Table 1. In each test, large volumes of feed solution (>2L) and draw solution

(>2L) were used. As only up to 5g water diffused across TFC membranes during each testing period, the salinity variations of the feed and draw solutions were negligible. Temperature of the draw solution was maintained at 25±1°C. The mass of the circulated feed stream was monitored by a digital data logging system.

[Table 1]

3. Theoretical simulation: mass transport across the membrane in PRO processes

[Fig. 2]

[Table 2]

A schematic diagram of the salt concentration profile across a TFC membrane under PRO is illustrated in Fig. 2. It has been shown by some prior works that the model for a radial geometry converges with the model developed for a flat geometry when the fiber radius increases [24, 30]. Furthermore, the model for a flat geometry can be employed for hollow fiber membranes if an equivalent thickness of the hollow fibers is used for the determination of the structural parameter [30]. Based on the inner diameter (ID) and outside diameter (OD) of the inner- and outer-selective hollow fiber membranes given in Table 2, for both membranes, the support layer thickness is 2 to 3 times less than the membrane ID and OD, respectively. Meanwhile, the selective layer is typically less than 300nm for TFC hollow fiber membranes [22, 25]. Since both the selective layer and the supportive layer are much thinner than the diameter of hollow fibers, one-dimensional coordinate is used in this work [8, 14]. Assuming ECP in the draw solution side is negligible due to efficient mixing, the effects of ICP within the porous support and the reverse salt flux across the membrane are the main causes resulting in a smaller effective osmotic driving force ($\Delta\pi_{eff}$) than the bulk osmotic driving force ($\Delta\pi_b$) [28]. Water flux can be computed as follows [28, 29]:

$$J_w = A\left(\Delta\pi_{eff} - \Delta P\right) = A(\pi_{D,m} - \pi_{F,m} - \Delta P) \quad (4)$$

in which $\pi_{D,m}$ and $\pi_{F,m}$ are the osmotic pressures of the draw and feed solutions facing the selective layer surfaces, respectively. The salt flux across the selective layer (J_s) can be written as [28]

$$J_s = B\left(C_{D,m} - C_{F,m}\right) \quad (5)$$

in which $C_{D,m}$ and $C_{F,m}$ are the salt concentrations of the draw and feed solutions at the selective layer surfaces, respectively. Meanwhile, the salt flux across the porous support comprises two components: a diffusive part due to the salt concentration gradient, and a convective part due to the bulk flow induced by J_w [28, 31]

$$J_s = \frac{D\varepsilon}{\tau}\frac{dC(x)}{dx} - J_w C(x) \quad (6)$$

where ε and τ are the porosity and tortuosity of the porous support, respectively. D is the salt diffusivity. At steady state, the salt flux across the selective layer (Eq. 5) is equal to the salt flux across the porous support (Eq. 6):

$$B\left(C_{D,m} - C_{F,m}\right) = \frac{D\varepsilon}{\tau}\frac{dC(x)}{dx} - J_w C(x) \quad (7)$$

The boundary conditions for Eq. 7 are:

at x=0, $C(x)=C_{F,b}$

at $x=t_s$, $C(x)=C_{F,m}$

where t_s is the thickness of the porous support and $C_{F,b}$ is the salt concentration of the bulk feed solution. Eq. 7 can be integrated to give:

$$C(x) = C_{F,b}\exp\left(J_w K \cdot \frac{x}{t_s}\right) + \frac{J_s}{J_w}\left[exp\left(J_w K \cdot \frac{x}{t_s}\right) - 1\right] \quad (8)$$

and [28]

$$\frac{C_{F,m}}{C_{D,m}} = \frac{B[exp(J_w K) - 1] + J_w(C_{F,b}/C_{D,m})exp(J_w K)}{B[exp(J_w K) - 1] + J_w} \quad (9)$$

Where K is defined as $\frac{\tau t_s}{D\varepsilon}$, referring to the resistance to the salt transport in the porous support. Combining Eq. 4 and Eq. 9, one can have:

$$J_w = A\left[\frac{\pi_{D,m} - \pi_F exp(J_w K)}{1 + \frac{B}{J_w}[exp(J_w K) - 1]} - \Delta P\right] \quad (10)$$

in which π_F is the osmotic pressure of the bulk feed solution. Power density (PD) can be obtained by:

$$PD = \frac{J_w \Delta P}{36} \quad (11)$$

in which water flux (J_w), operation pressure (ΔP) and power density (PD) are in the unit of L/m^{2}h (LMH), bar, and W/m^2, respectively. When ΔP=0, Eq. 10 can be rearranged as follows:

$$J_w = \frac{1}{K} ln\left(\frac{A\pi_{D,m} - J_w + B}{A\pi_F + B}\right) \quad (12)$$

Similarly, Eq. 13 can be rewritten as follows for the FO mode (i.e., the selective layer faces the feed) at ΔP=0 [16, 22]:

$$J_w = \frac{1}{K} ln\left(\frac{A\pi_D + B}{A\pi_{F,m} + J_w + B}\right) \quad (13)$$

From the solute resistivity K, the structural parameter (S) can be determined:

$$S = KD \quad (14)$$

in which S is related to the tortuosity (τ), thickness (t_s), and porosity (ε) of the porous support by Eq. 15:

$$S = \frac{\tau t_s}{\varepsilon} \tag{15}$$

Then based on Eq. 8, the salt concentration of the feed at the selective layer surface ($C_{F,m}$) can be expressed as follows:

$$C_{F,m} = C_{F,b}\underbrace{\exp\left(\frac{J_w S}{D}\right)}_{\text{ICP factor}} + \frac{J_s}{J_w}\underbrace{\left[\exp\left(\frac{J_w S}{D}\right) - 1\right]}_{\text{equivalent ICP factor}} \tag{16}$$

ICP contribution J_s contribution

Eq. 16 indicates that $C_{F,m}$ comprises two terms. The first term represents the contributions from the internal factors (i.e., concentrative ICP and others) and is referred to as the ICP contribution. The second term stands for the contributions from the reverse salt permeation across the selective layer and is thereafter called as the Js contribution. J_s/J_w is the specific reverse salt flux. As J_s/J_w has a concentration unit, it can be considered as an equivalent concentration induced by the reverse salt permeation. The percentage of the J_s contribution to $C_{F,m}$ is defined as J_s-contribution %:

$$J_s\text{-contribution } \% = \frac{J_s \text{ contribution}}{C_{F,m}} \times 100\% \tag{17}$$

Table 2 summarizes the inner diameter (ID), outside diameter (OD), water permeability (A), reverse salt permeability (B) and structural parameter (S) of the inner- and outer-selective membranes used in this study. It is worth noting that A and B values of the outer-selective membrane are smaller compared to those of the inner-selective membrane. As reported in prior works [7, 17, 21], a pre-stabilization step were often applied to the inner-selective membranes to improve their performance. For example, before the PRO tests, a high pressure

of 20 bar was applied to the lumen side of the inner-selective membrane for 30 min [8]. The pre-stabilization not only improved the water permeability, but also reduced the structural parameter due to the membrane expansion induced by the high pressure [7]. At the same time, the salt permeability was also moderately increased [7]. The outer-selective membrane did not have such per-stabilization step. In fact, since the operation pressure was applied from outside the membrane, the selective layer of the outer-selective membrane was compressed during PRO operations. Moreover, although selective layers of both membranes were formed via interfacial polymerization, the detailed fabrication processes were different from each other [8, 25]. For example, during the fabrication of the outer-selective membrane, the employment of vacuum at 800 mbar could effectively remove the excess amine solution, which is often considered as the key step to fabricate an almost defect-free selective layer with a low salt permeability [25]. Therefore, the outer-selective membrane has smaller A and B values.

4. Results and discussion

4.1 Comparison between inner- and outer-selective TFC hollow fiber membranes under a fixed bulk salinity gradient

To study the relationship among the internal factors and their effects on the external performance, a 0.81M NaCl aqueous solution was used as the draw solution, which has the same osmolality as the first-stage RO brine of a local RO plant. A 0.011 M NaCl aqueous solution was used as the feed, which has the same osmolality as the wastewater retentate obtained from a local wastewater plant [8].

[Fig. 3]

Fig.3 (1a) to Fig.3 (2f) show various internal factors (J_s, J_s contribution, $C_{F,m}$, ICP contribution, $\Delta\pi_{eff}$, J_s/J_w and others) and external performance indices (J_w and PD) as a function of operation pressure (ΔP). As illustrated in Fig.3 (1a) and (2a), reverse salt fluxes (J_s) of both membranes increase with operation pressure (ΔP) under the fixed bulk salinity gradient. However, the inner-selective membrane has J_s values about ten times higher than the outer-selective one due to its higher B value. Interestingly, for both membranes, the J_s contribution exhibits a convex trend and reaches a peak at a certain operation pressure less than 15bar. To explain the trend, let's use the outer-selective membrane as an example. As defined in Eq. 16, the J_s contribution is a product of the J_s/J_w ratio and the equivalent ICP factor. Since J_s increases rapidly with ΔP in the range of 0 to 9 bar as shown in Fig.3 (1a), while J_w decreases relatively slowly at the low ΔP range (Fig.3 (1e)), these result in a slow reduction of the equivalent ICP factor. Therefore, the growth of J_s /J_w overwhelms the reduction of the equivalent ICP factor, leading to a peak in the J_s contribution profile at 9 bar. When ΔP is higher than 9 bar, the J_s contribution starts to decay due to the dominant reduction of the equivalent ICP factor.

Based on Eq. 4, water flux at a given ΔP is determined by the effective osmotic pressure difference ($\Delta\pi_{eff}$) and water permeability (A). As $\Delta\pi_{eff}$ is proportional to the salinity gradient across the selective layer (i.e., $\Delta C_m = C_{D,m} - C_{F,m}$), it is important to investigate the behaviours of $C_{F,m}$ and its component factors defined in Eq. 16. As plotted in Fig.3 (1b) and (2b), the ICP contribution of both membranes monotonically decrease in the entire ΔP range, while the J_s contribution exhibits a convex trend. As the reduction of the ICP contribution is dominant, $C_{F,m}$ exhibits a monotonic decline. Consequently, $\Delta\pi_{eff}$ increases with an increase in ΔP (Fig.3 (1c) and (2c)), so does J_s because of Eq. 5. Since the inner-selective membrane

has a much higher B value than the outer-selective one, the former has a more significant J_s contribution than the latter, as illustrated in Fig.3 (1b) vs. (2b). As a consequence, the effects of reverse salt permeation on PRO performance are more severe for the inner-selective membrane. For example, the inner-selective membrane at 20 bar has a J_s/J_w value about 5 times higher than the outer-selective membrane. The former also has a J_s-contribution % more than 3 times higher than the latter.

Comparing Fig.3 (1b) and (2b), one can find that, although the inner-selective membrane has a much larger J_s contribution, its $C_{F,m}$ is only slightly higher than that of the outer-selective membrane. Consequently, as shown in Fig.3 (1c) vs. (2c), its $\Delta\pi_{eff}$ curve is only slightly below the curve of the outer-selective membrane. This is due to the fact that the effect of its large B is effectively offset by its small S value (i.e., small ICP factor and the equivalent ICP factor). As J_w is determined by $\Delta\pi_{eff}$ and A, the inner-selective membrane still outperforms the outer-selective membrane in terms of J_w and power density because the former has a higher A value than the latter, as evidenced when comparing Fig.3 (1e) vs. (2e) and (1f) vs. (2f).

4.2 Comparison between inner- and outer-selective TFC hollow fiber membranes under a growing bulk salinity gradient

Prior investigations under the fixed bulk salinity gradient have established an effective approach to analyse the relationships among various internal factors and their effects on the external performance. In reality, due to the water permeation into the draw solution and undesirable reverse flux to the feed, the bulk feed salinity ($C_{F,b}$) will increase along membrane modules. Therefore, it is meaningful to examine how internal factors response to

this growing bulk salinity gradient. In the following discussion, the draw solution has a fixed bulk salinity of 0.81 M NaCl and the operation pressure is set at 20 bar.

[Fig. 4]

The relationship between reverse salt flux (J_s) and feed bulk salinity ($C_{F,b}$) is presented in Fig. 4 (a). As the interface salinity ($C_{F,m}$) increases with the feed salinity ($C_{F,b}$) (Fig. 4 (b)), the reverse salt flux (J_s) decreases with $C_{F,b}$.The inner-selective membrane exhibits a much higher J_s than the outer-selective membrane due to its large B value. Interestingly, as shown in Fig. 4 (c), despite of the reducing J_s, the J_s/J_w ratio keeps growing with $C_{F,b}$ for both membranes. This trend can be explained by Eq. 18.

$$\frac{J_s}{J_w} = \frac{B\Delta C_m}{A(iRT\Delta C_m - \Delta P)} = \frac{B}{A(iRT - \frac{\Delta P}{\Delta C_m})} \quad (18)$$

where ΔC_m is the salinity gradient across the selective layer of the membrane (i.e., ΔC_m = $C_{D,m}$ - $C_{F,m}$), i is the van't Hoff coefficient, R is the universal gas constant, and T is the absolute temperature. On one hand, as ΔC_m decreases with increasing $C_{F,b}$, J_s/J_w increases with $C_{F,b}$ because ($iRT\Delta C_m$-ΔP) in the denominator decreases faster than ΔCm in the numerator. On the other hand, the growth rate of J_s/J_w depends on the B/A ratio, which can be considered as the reciprocal of the membrane selectivity. As the B/A ratio of the inner-selective membrane is much larger than that of the outer-selective membrane (i.e., 0.086 bar vs. 0.020 bar), the inner-selective membrane presents a more rapid growth of J_s/J_w.

The trend of $C_{F,m}$ and its ICP contribution are illustrated in Fig.4 (b). Using the inner-selective membrane as an example, one can find that both $C_{F,m}$ (represented by line section $\overline{AC}$) and its ICP contribution (represented by $\overline{BC}$) increases monotonically with $C_{F,b}$.

Meanwhile, the gap between the two curves (i.e., J_s contribution, represented by $\overline{AB}$) decreases with $C_{F,b,}$ which is consistent with the trend of J_s-contribution % in Fig.4 (d). Comparing to the inner-selective membrane, the curves of ICP contribution and $C_{F,m}$ of the outer-selective membrane are close to each other because its J_s contribution is effectively suppressed by its low B value. As shown in Fig.4 (d), the contribution of its J_s contribution to $C_{F,m}$ (i.e., J_s-contribution %) is less than 10% when $C_{F,b}$ is larger than 0.01M.

Fig.4 (e) and (f) show the effective driving force ($\Delta\pi_{eff}$) and water flux (J_w) as a function of $C_{F,b}$. For both membranes, $\Delta\pi_{eff}$ decreases rapidly with an increase in $C_{F,b}$ (Fig.4 (b)). As a result, water flux declines rapidly with an increase in $C_{F,b}$, especially in the low $C_{F,b}$ range up to 0.01M. This implies that power density will drop drastically when employing low salinity feeds such as RO treated MBR permeate as the feed in PRO [8, 15]. Since the feed has a salinity of 0.011M in this study, the inner-selective membrane exhibits faster drops in both water flux and power density compared to the outer-selective membrane. For example, when $C_{F,b}$ increases from 0.011M to 0.03M, the power density of the inner-selective membrane drops by 4.4W/m^2 (represented by line $\overline{CD}$) while that of the outer-selective membrane drops by only 2.2 W/m^2 (represented by $\overline{C'D'}$). In summary, since $C_{F,b}$ is typically equal or larger than 0.01M in real applications, the effect of the ICP contribution on $C_{F,m}$ would become dominant with growing $C_{F,b}$, as illustrated in Fig.4 (b). This would result in fast declines in both water flux and power density (Fig.4 (f)).

4.3 Gypsum scaling in the TFC hollow fiber membrane

When the feed pair contains scaling precursors, the performance of TFC hollow fiber membranes will not only drop due to the growing salinity in the feed, but also deteriorate by

severe scaling within the membrane [11, 15]. In this work, the outer-selective TFC hollow fiber membrane is used to investigate the underlying mechanism of the gypsum scaling. Fig.5 (a) plots the weight loss profiles of the feed as a function of time under different bulk saturation indices (SI). The scaling process can be divided into two stages: (1) an initial rapid decline stage with a slightly concave trend from their original starting points to points A, A' and A", and (2) then an approximately linear stage. Weight loss profiles can be further translated into water flux curves as illustrated in Fig.5 (b) and (c). Four classical flux decline models listed in Table 3 [32, 33] are employed to fit the water flux curves in order to examine their patterns and divide them into more detailed stages. As shown in Fig.5 (b), the best fitting is achieved by the modified pore blocking model. Therefore, as shown in Fig.5 (c), the water flux curves can hypothetically be divided into three stages: (1) an initial exponentially descending stage (for example, from the starting point up to point B) (2) a transition stage, and (3) a final pseudo-stable stage (for example, the profile after point A).

[Table 3]

[Fig. 5]

To examine the relationship between pore blocking and subsequent flux reduction behaviour, the distributions of scaling precursors within the porous support are estimated based on Eq. 8 and plotted in Fig.5 (d). The concentrations of scaling precursors grow relatively slowly at positions near the porous support surface facing the bulk feed (i.e., the locations near x=0), and progressively increase when approaching to the interface between the porous support and the selective layer (i.e., the location near $x=t_s$). The local saturation index (SI) displays a similar trend accordingly. Based on the advanced nucleation theory [34-39], the relationship among nucleation barrier (ΔG^*), nucleation rate (J) (i.e., the population of critical nuclei

generated per unit-volume and unit-time), and critical radius of nuclei (r_c) can be described as:

$$\Delta G^* = \frac{16\pi r_{cf}^3 \Omega^3}{3[kTln(1+\sigma)]^2} \quad (19)$$

$$J = B' exp\left(-f\frac{\Delta G^*}{kT}\right) \quad (20)$$

$$r_c = \frac{2\Omega r_{cf}}{kTln(1+\sigma)} \quad (21)$$

where k is the Boltzmann constant, T is the absolute temperature, r_{cf} is the surface free energy between the nuclei and the mother phase, Ω is the volume of the growth unit and B' is a kinetic parameter which is constant for a given system. f ($0 \leq f \leq 1$) is a factor describing the reduction of the nucleation barrier due to a foreign body. σ is the supersaturation which can be well represented by SI [36, 37, 39]:

$$\ln(1+\sigma)=\ln(IAP/K_{sp})=\ln(SI) \quad (22)$$

SI is the saturation index defined as IAP/K_{sp}, in which IAP is the product of the precursor ion activities and K_{sp} is the solubility constant of gypsum. Clearly, a higher local SI value leads to a higher local supersaturation and hence a lower nucleation barrier. This will promote a larger nucleation rate of the critical nuclei with a smaller size. As the local SI value changes with different locations inside the membrane, nucleation rate and nuclei size also change with different locations accordingly. With these insights in mind, Fig. 6 schematically illustrates the possible mechanisms of flux decline in the scaling process.

[Fig. 6]

Once scaling is initiated, scaling precursors such as Ca^{2+} and SO_4^{2-} will soon build up inside the membrane porous support due to the effect of concentrative ICP. As illustrated in the inset (I) of Fig. 6, in the region just beneath the selective layer, a large population of small

critical nuclei may be generated either on the selective layer through surface crystallization (i.e., heterogeneous nucleation) or from the mother phase through homogeneous-like nucleation [34, 35, 40, 41]. The nuclei in the mother phase may rapidly deposit underneath the selective layer due to the local water flux toward the selective layer induced by the draw solution. These deposited nuclei, together with the nuclei produced by surface crystallization, occupy a certain portion of the selective layer surface, leading to instant losses of water permeability (A) and water flux (J_w). Such surface coverage can be verified by DI water backwash performed at 15 bar immediately after every scaling test. If water flux can be quickly recovered after the backwash, surface crystallization and surface deposition are less severe. On the contrary, if it takes a certain period of time to recover water flux, then the surface crystallization is more severe and the nuclei deposition is more compact. Experimental results indicate that an instant recovery of nearly 100% water flux can be achieved after backwash when using a feed bulk SI of 1.01 for the scaling test. In contrast, the recovery of the initial water flux is only 85% if a feed bulk SI of 2.06 is employed. It takes 30 minutes to fully recover the water flux. Such different responses to the backwash may be due to the following reasons. Since the actual space available for the initial fast nucleation underneath the selective layer in the asymmetric membrane support is highly constricted, a higher feed bulk SI value would lead to a larger local supersaturation near the selective layer and result in nuclei with a smaller size. Therefore, a feed with a higher SI value would facilitate the deposition and form a more compact crystalline layer. Consequently, as shown in Fig.5 (c), one can observe a steeper initial flux reduction for the case of SI=2.06 and less steep initial flux drops for SI=0.43 and SI=1.01.

After the rapid surface crystallization and nuclei deposition, quick stacking or bridging may occur in the porous substrate a bit far away from the selective layer, as illustrated in the inset

(II) of Fig. 6. Owing to the high supersaturation in the mother phase, nucleation is rather fast in this regime and the nascent nuclei size is still small due to the low nucleation barrier at the high local supersaturation. These small crystals may quickly block the flow channels in the membrane porous support. Not only do they induce a quick growth of tortuosity (τ) but also a fast decline of porosity (ε). Therefore, the structural parameter (S) increases rapidly and the initial flux declines exponentially because of the drastically enhanced ICP. This flux behaviour can be further supported by Fig. 7 (will be discussed in details later). After a certain period of time t_l, fast nucleation near the selective layer is almost complete, growth of S is then dominated by the relatively slower nucleation with larger nuclei sizes occurring in the region further away from the selective layer, as illustrated by the inset (III). Meanwhile, the previously mentioned regions adjacent to the selective layer (corresponding to insets (I) and (II)) enters the crystal growth stage. Comparing to nucleation, crystal growth is relatively sluggish and provides less contributions to the growth of S. As illustrated in the inset (III), because nucleation rate in the transition stage slows down, the water flux decline also slows down. Finally, when nucleation comes to the end for all the regions inside the porous support, crystal growth eventually takes over as the dominant role. A sluggish S growth coupling with a very slow water flux decline leads to an apparently pseudo-stable stage, as illustrated by the inset (IV) in Fig. 6.

Based on the above analysis, one may have a better understanding of Fig.5 (c). Among the three curves, the feed with a SI value of 2.06 has the fastest growth in structural parameter due to the largest local supersaturation inside the porous support. As a result, it has earlier turning points between these three stages such as points B" and A" than the other two cases. On the other hand, it also has the smallest gypsum nuclei size because it has the largest local supersaturation within the membrane. The combination of these two factors would result in

the fouled membrane with the densest gypsum scaling inside the porous support, the largest S growth and the lowest water flux compared to the other two cases. However, if the scaling process continues for a sufficiently long period of time, all three curves in Fig.5 (c) would merge together as reported in some prior works [26, 42]. This phenomenon implies that the initial exponentially declining stage and the following transition stage in Fig. 6 may be termed as "foulant-membrane interaction". Similar to those pressurized filtration processes such as NF and RO [26, 42], scalants interact with the membrane in these stages resulting in a significant change of membrane structural parameter through nucleation. The final pseudo-stable stage can be named as "foulant-foulant interaction" [26, 42] because gypsum crystal growth is dominant in this stage. Nevertheless, kinetics of scaling in PRO is still much different from those of pressurize-driven filtration processes in nature.

5. Implications and perspectives

5.1 TFC hollow fiber membranes

This study may provide useful insights to design suitable membranes for PRO applications. Since inner- and outer-selective TFC hollow fiber membranes deform differently under high-pressure PRO operations, different design strategies may be adopted for their membrane fabrication. Although the outer-selective TFC hollow fiber membrane benefits from its low salt permeability, it suffers from (1) low water flux due to its relatively low water permeability and large structural parameter and (2) compaction effects from the hydraulic pressure in the shell side. A significant improvement on its water permeability while remaining its low salt permeability requires breakthroughs in current techniques of interfacial polymerization and membrane materials. One should reduce its structural parameter by learning some insights from the formation of inner-selective hollow fiber membranes and enhance membrane robustness by adopting some concepts from nano-composite materials.

Fig. 7 shows the water flux as a function of structural parameter for the outer-selective membrane. Similar to the typical viscosity curves of polymer solutions as a function of shear rate [43, 44], there exists a critical structural parameter (S^c). In the range of $S<S^c$, a reduction of structural parameter can significantly enhance the water flux. As elucidated in Fig. 8, a small structural parameter can remarkably enlarge the effective driving force ($\Delta\pi_{eff}$) (Fig.8 (a)), enhance water flux (Fig.8 (b)), and improve power density (Fig.8 (c)).

[Fig. 7]

[Fig. 8]

As for the inner-selective membrane, it seems to be superior in terms of water flux and power density under the constant bulk salinity gradient (Fig.8 (b) and (c)). Its performance is so close to the virtual 'perfect' membrane, which combines strong points from both inner and outer-selective membranes (i.e., A=3.5LMH/bar, B=0.028LMH, and S=450μm). However, as pointed out in earlier discussions, the performance of the inner-selective membrane is weakened because of the growing bulk salinity gradient. To maintain its performance, great efforts must be given to lower its B value in order to mitigate the severe effect of reverse flux. In summary, efforts to molecularly design the interfacial polymerization with a high A and a lower B, micro-morphologically control the substrate's inner skin suitable for a defect-free polyamide layer, and optimize the pre-stabilization step are needed [7, 18, 20].

5.2 TFC hollow fiber membranes used in real PRO applications

Besides river water, the retentate from municipal wastewater plants is another promising feed water candidate for PRO processes, especially in the countries of scarcity in river water. Wastewater retentate can be the rejected stream from a low pressure RO process where MBR permeate is used as the feed. It may consist of inorganic compounds with a total dissolved

solid (TDS) of about 1000mg/L and a total organic carbon (TOC) of 44ppm [8]. For such kind of feed, scaling may play a dominant role in membrane fouling [8, 12, 15]. Fig. 9 demonstrates the water flux declining curves when a local wastewater retentate is employed as the feed and a 0.81M NaCl solution is used as the draw solution. Similar to the curves discussed in the gypsum scaling study, the best fitting is achieved by the modified pore blocking model. The water flux drops drastically in the initial stage followed by a transition stage and a final pseudo-stable stage. It is worth noting that, comparing to the curve operated at 20 bar, the water flux decline in the initial stage at 10 bar is steeper due to the more severe scaling at the higher water flux.

[Fig. 9]

For both inner- and outer-selective membranes, water flux decreases when the feed of DI water is replaced by other low salinity feeds or wastewater retentate. As illustrated in Fig. 10, the difference in water flux between these two membranes is getting smaller as a function of feed salinity and almost diminishes due to severe scaling when a wastewater retentate is used as the feed.

[Fig. 10]

To mitigate scaling, future research works may focus on (1) the removal of scaling precursors in feed streams by developing cost-effective pre-treatments such as (1) low pressure NF and RO [8], (2) exploring low cost anti-scalants [12, 15], and (3) developing anti-scaling TFC hollow fiber membranes [45-48].

6. Conclusion

By using both inner- and outer-selective PRO membranes, we have studied the relationship among the internal factors and their effects on the external performance of PRO processes.

As elucidated in Fig. 11, both the water flux and the reverse salt flux are ultimately linked to the same internal factor: the salinity gradient across the selective layer (ΔC_m). With negligible ECP, ΔC_m is determined by the surface salinity on the feed side ($C_{F,m}$). $C_{F,m}$ comprises two terms with two associated factors. One is the bulk concentration $C_{F,b}$ and the ICP factor, while the other is the equivalent concentration J_s/J_w and the equivalent ICP factor. Membrane properties such as A, B, S and operation parameters such as ΔP and $C_{F,b}$ take effect at different locations in the framework, resulting in various external performance behaviours. When the feed pair contains negligible fouling tendency, external performance indices are mainly determined by $C_{F,m}$, (i.e., $C_{F,b}$ and J_s/J_w amplified by their associated factors). When the feed pair contains scaling precursors, external performance is severely affected by the drastic changes in their associated factors through S. This study may provide a bottom-up perspective facilitating a comprehensive understanding of the mechanisms behind various external performance behaviours.

[Fig. 11]

Acknowledgements

This research study is supported by the National Research Foundation, Prime Minister's Office, Republic of Singapore, under its Environmental & Water Technologies Strategic Research Programme and administered by the Environment & Water Industry Programme Office (EWI) of the PUB. This research work was funded by the project entitled "Membrane development for osmotic power generation, Part 2, Module fabrication and system integration" (1102-IRIS-11-02) and NUS Grant Number of R-279-000-382-279. The authors also would like to thank Dr. X. Li, Dr. G. Han, Dr. S. Zhang and Mr. F. J. Fu for fruitful discussions, Mr T. S. Yang and Mr D. J. Cai for their supports in experiments, and Ms S. H. An for the improvement of the writing.

Nomenclature

DI water	deionized water
ECP	external concentration polarization
ICP	internal concentration polarization
MBR	membrane bioreactor
MPD	m-phenylenediamine
NF	nanofiltration
PES	polyethersulfone
PRO	pressure retarded osmosis
RO	reverse osmosis
SDS	sodium dodecyl sulfate
SI	saturation index
TFC	thin film composite
TMC	1,3,5- benzenetricarboxylic acid chloride
TOC	total organic carbon
A	water permeability (LMH/bar)
A_m	effective membrane area (m^2)
B	reverse salt permeability (LMH)
B'	kinetic parameter for a given nucleation system (-)
$C_{D,b}$	salinity of the bulk draw solution (M)
$C_{D,m}$	surface salinity of the selective layer at the draw solution side (M)
C_f	salt concentration of the feed (ppm)
$C_{F,b}$	salinity of the bulk feed solution (M)
$C_{F,m}$	surface salinity of the selective layer at the feed side (M)
ΔC_m	salinity gradient across the selective layer of the membrane (M)
C_p	salt concentration of the permeate (ppm)
D	salt diffusivity in water (m^2/s)
f	factor describing the reduction of nucleation barrier due to a foreign body (-)
ΔG^*	nucleation barrier (J)
i	Van't Hoff coefficient
IAP	the product of precursor ion activities (-)
J	nucleation rate (-)
J_w	water flux (LMH)
J_s	reverse salt flux (gMH)
J_s/J_w	specific reverse salt flux (M)
k	Boltzmanns constant ($1.3806488 \times 10^{-23}$ $J.K^{-1}$)
K_{sp}	solubility constant of gypsum (-)
PD	power density (W/m2)
ΔP	operation pressure (bar)
r_c	radius of critical nuclei (m)
r_{cf}	surface free energy between the nuclei and the mother phase (N/m)
R	universal gas constant (0.083145 $L.bar.mol^{-1}.K^{-1}$)
R_s	salt rejection (%)
S	structural parameter (μm)
S^c	critical structural parameter (μm)
t_I	duration of initial exponentially descending stage of water flux curves (h)
t_{II}	duration of transition stage of water flux curves (h)
t_{III}	duration of final pseudo-stable stage of water flux curves (h)

t_s	thickness of the membrane porous support (μm)
Δt	the period of time used to collect permeate (h)
T	absolute temperature (K)
TDS	total dissolved solid (mg/L)
ΔV	the permeate volume collected over a certain period of time (L)
x	certain position within the membrane porous support (μm)
$\Delta\pi$	osmotic pressure difference across the membrane (bar)
$\Delta\pi_b$	osmotic pressure difference between the bulk draw solution and the bulk feed solution (bar)
π_D	osmotic pressure of the bulk draw solution (bar)
$\Delta\pi_{eff}$	effective osmotic pressure difference across the selective layer of the membrane (bar)
π_F	osmotic pressure of the bulk feed solution (bar)
Ω	the volume of the growth nucleation unit (m^3)
σ	supersaturation (-)
ε	porosity of the porous support (-)
τ	tortuosity of the porous support layer (-)

References

[1] T. Thorsen, T. Holt, The potential for power production from salinity gradients by pressure retarded osmosis, J. Membr. Sci. 335 (2009) 103-110.
[2] A. Evans, V. Strezov, T.J. Evans, Assessment of sustainability indicators for renewable energy technologies, Renew. Sustain. Energy Rev. 13 (2009) 1082-1088.
[3] A. Achilli, T.Y. Cath, A.E. Childress, Power generation with pressure retarded osmosis: an experimental and theoretical investigation. J. Membr. Sci. 343 (2009) 42-52.
[4] T.S. Chung, X. Li, R.C. Ong, Q. Ge, H. Wang, G. Han, Emerging forward osmosis (FO) technologies and challenges ahead for clean water and clean energy applications, Curr. Opin. Chem. Eng. 1 (2012) 246-257.
[5] B.E. Logan, M. Elimelech, Membrane-based processes for sustainable power generation using water, Nature 488 (2012) 313-319.
[6] Z. Jia, B. Wang, S. Song, Y. Fan, Blue energy: Current technologies for sustainable power generation from water salinity gradient, Renew. Sustain. Energy Rev. 31 (2014) 91-100.
[7] G. Han, S. Zhang, X. Li, T.S. Chung, Progress in pressure retarded osmosis (PRO) membranes for osmotic power generation, Prog. Polym. Sci. 51 (2015) 1–27.
[8] C.F. Wan, T.S. Chung, Osmotic power generation by pressure retarded osmosis using seawater brine as the draw solution and wastewater retentate as the feed, J. Membr. Sci. 479 (2015) 148-158.
[9] Q. She, X. Jin, C.Y. Tang, Osmotic power production from salinity gradient resource by pressure retarded osmosis: Effects of operating conditions and reverse solute diffusion, J. Membr. Sci. 401–402 (2012) 262-273.
[10] Q. She, Y.K.W. Wong, S. Zhao, C.Y. Tang, Organic fouling in pressure retarded osmosis: Experiments, mechanisms and implications, J. Membr. Sci. 428 (2013) 181-189.
[11] M. Zhang, D. Hou, Q. She, C.Y. Tang, Gypsum scaling in pressure retarded osmosis: Experiments, mechanisms and implications, Water Res. 48 (2014) 387-395.

[12] D.I. Kim, J. Kim, H.K. Shon, S. Hong, Pressure retarded osmosis (PRO) for integrating seawater desalination and wastewater reclamation: Energy consumption and fouling, J. Membr. Sci. 483 (2015) 34-41.
[13] J. Kim, J. Lee, J.H. Kim, Overview of pressure-retarded osmosis (PRO) process and hybrid application to sea water reverse osmosis process. Desalin. Water Treat. 43 (2012) 193-200.
[14] S. Zhang, T.S. Chung, Minimizing the instant and accumulative effects of salt permeability to sustain ultrahigh osmotic power density, Environ. Sci. Technol. 47 (2013) 10085-10092.
[15] S.C. Chen, G.L. Amy, T.S. Chung, Membrane fouling and anti-fouling strategies using RO retentate from a municipal water recycling plant as the feed for osmotic power generation, Water Res. 88 (2016) 144-155.
[16] N.Y. Yip, A. Tiraferri, W.A. Phillip, J.D. Schiffman, L.A. Hoover, Y.C. Kim, M. Elimelech, Thin-Film Composite pressure retarded osmosis membranes for sustainable power generation from salinity gradients, Environ. Sci. Technol. 45 (2011) 4360-4369.
[17] X.X. Song, Z.Y. Liu, D.D. Sun, Energy recovery from concentrated seawater brine by thin-film nanofiber composite pressure retarded osmosis membranes with high power density, Energ. Environ. Sci., 6 (2013) 1199-1210.
[18] Y. Cui, X.Y. Liu, T.S. Chung, Enhanced osmotic energy generation from salinity gradients by modifying thin film composite membranes, Chem. Eng. J. 242 (2014) 195-203.
[19] S. Chou, R. Wang, A.G. Fane, Robust and high performance hollow fiber membranes for energy harvesting from salinity gradients by pressure retarded osmosis, J. Membr. Sci. 448 (2013) 44-54.
[20] S. Zhang, P. Sukitpaneenit, T. S. Chung, Design of robust hollow fiber membranes with high power density for osmotic energy production, Chem. Eng. J. 241 (2014) 457-465.
[21] G. Han, P. Wang, T. S. Chung, Highly robust thin-film composite pressure retarded osmosis (PRO) hollow fiber membranes with high power densities for renewable salinity-gradient energy generation, Environ. Sci. Technol. 47 (2013) 8070-8077.
[22] X. Li, T.S. Chung, Thin-film composite P84 co-polyimide hollow fiber membranes for osmotic power generation, Appl. Energ. 114 (2014) 600-610.
[23] N.N. Bui, J.R. McCutcheon, Nanofiber supported thin-film composite membrane for pressure-retarded osmosis, Environ. Sci. Technol. 48 (2014) 4129-4136.
[24] E. Sivertsen, T. Holt, W.R. Thelin, G. Brekke, Iso-watt diagrams for evaluation of membrane performance in pressure retarded osmosis, J. Membr. Sci. 489 (2015) 299-307.
[25] Z.L. Cheng, X. Li, Y. Liu, T.S. Chung, Robust outer-selective thin-film composite polyethersulfone hollow fiber membranes for osmotic power generation, J. Membr. Sci. accepted (2015).
[26] C.Y. Tang, T.H. Chong, A.G. Fane, Colloidal interactions and fouling of NF and RO membranes: A review, Adv. Colloid Interface Sci. 164 (2011) 126-143.
[27] C.Y. Tang, J.O. Leckie, Membrane independent limiting flux for RO and NF membranes fouled by humic acid, Environ. Sci. Technol. 41 (2007) 4767-4773.
[28] K. Lee, R. Baker, H. Lonsdale, Membranes for power generation by pressure-retarded osmosis, J. Membr. Sci. 8 (1981) 141-171.
[29] H.K. Lonsdale, Recent advances in reverse osmosis membranes, Desalination 13 (1973) 317-332.
[30] E. Sivertsen, T. Holt, W.R. Thelin, G. Brekke, Modelling mass transport in hollow fibre membranes used for pressure retarded osmosis, J. Membr. Sci. 417-418 (2012) 69-79.
[31] G. Han, S. Zhang, X. Li, T.S. Chung, High performance thin film composite pressure retarded osmosis (PRO) membranes for renewable salinity-gradient energy generation, J. Membr. Sci. 440 (2013) 108-121.

[32] L.J. Zeman, A.L. Zydney, I. NetLibrary, Microfiltration and ultrafiltration: principles and applications, M. Dekker, New York, 1996.
[33] M. Cheryan, Ultrafiltration handbook, Technomic Pub. Co, Lancaster, Pa, 1986.
[34] X.Y. Liu, Heterogeneous nucleation or homogeneous nucleation?, J. Chem. Phys. 112 (2000) 9949-9955.
[35] X.Y. Liu, Generic Progressive Heterogeneous Processes in Nucleation, Langmuir 16 (2000) 7337-7345.
[36] X.Y. Liu, K. Tsukamoto, M. Sorai, New Kinetics of $CaCO_3$ Nucleation and Microgravity Effect, Langmuir 16 (2000) 5499-5502.
[37] X.Y. Liu, Influence of nucleation nature on Ca mineral/substrate structural synergy and implications for biomineralization in microgravity, J. Chem. Phys. 115 (2001) 9970-9974.
[38] K.-Q. Zhang, X.Y. Liu, In situ observation of colloidal monolayer nucleation driven by an alternating electric field, Nature 429 (2004) 739-743.
[39] K. Sato, Y. Furukawa, K. Nakajima, Advances in crystal growth research, Elsevier Science, Amsterdam;New York;, 2001.
[40] S. Lee, C.-H. Lee, Effect of operating conditions on $CaSO_4$ scale formation mechanism in nanofiltration for water softening, Water Res. 34 (2000) 3854-3866.
[41] W.-Y. Shih, A. Rahardianto, R.-W. Lee, Y. Cohen, Morphometric characterization of calcium sulfate dihydrate (gypsum) scale on reverse osmosis membranes, J. Membr. Sci. 252 (2005) 253-263.
[42] C.Y. Tang, Y.-N. Kwon, J.O. Leckie, The role of foulant–foulant electrostatic interaction on limiting flux for RO and NF membranes during humic acid fouling—Theoretical basis, experimental evidence, and AFM interaction force measurement, J. Membr. Sci. 326 (2009) 526-532.
[43] T.S. Chung, S.K. Teoh, X. Hu, Formation of ultra-thin high-performance polyethersulfone hollow fiber membranes, J. Membr. Sci. 133 (1997) 161-175.
[44] N. Peng, T.S. Chung, K.Y. Wang, Macrovoid evolution and critical factors to form macrovoid-free hollow fiber membranes, J. Membr. Sci. 318 (2008) 363-372.
[45] X. Li, T. Cai, T.S. Chung, Anti-fouling behavior of hyperbranched polyglycerol-grafted poly(ether sulfone) hollow fiber membranes for osmotic power generation, Environ. Sci. Technol. 48 (2014) 9898-9907.
[46] P.H.H. Duong, T.S. Chung, S. Wei, L. Irish, Highly permeable double-skinned forward osmosis membranes for anti-fouling in the emulsified oil–water separation process, Environ. Sci. Technol. 48 (2014) 4537-4545.
[47] T. Cai, X. Li, C. Wan, T.S. Chung, Zwitterionic polymers grafted poly(ether sulfone) hollow fiber membranes and their antifouling behaviors for osmotic power generation, J. Membr. Sci. 497 (2016) 142-152.
[48] W. Fang, C. Liu, L. Shi, R. Wang, Composite forward osmosis hollow fiber membranes: Integration of RO- and NF-like selective layers for enhanced organic fouling resistance, J. Membr. Sci. 492 (2015) 147-155.

Solution ID	Feed Bulk SI	NaCl (mM)	$CaCl_2$ (mM)	Na_2SO_4 (mM)	Osmotic Pressure (bar)

1	0.43	105	10	20	7.44
2	1.01	67	15	40	7.41
3	2.06	16.5	24	65	7.44

Table 1. The solution compositions prepared for PRO gypsum scaling studies. Saturation Index (SI) is defined as IAP/K_{sp}, in which IAP is the product of the precursor activities (Ca^{2+} and SO_4^{2-}) and K_{sp} is the solubility constant of gypsum. The feed bulk SI was calculated by Aqion 5.8.1 software using the U.S.G.S. software PhreeqC as an internal numerical solver.

TFC Membrane	ID/OD (mm)	A (LMH/bar)	B (LMH)	S (μm)
outer-selective	0.53/1.1	1.42	0.028	996
inner-selective	0.58/1.0	3.50	0.30	450

Table 2. The inner diameter (ID), outside diameter (OD), pure water permeability (A), salt permeability (B), and structural parameter (S) of the outer-selective and inner-selective TFC hollow fiber membranes used in this study.

Classical Models	Model Equations	Parameters for Data Fitting
cake filtration	$J_w = J_0(1+bt)^{-1/2}$	J_0 (initial water flux), b
pore constriction	$J_w = J_0(1+bt)^{-2}$	J_0 (initial water flux), b
traditional pore blocking	$J_w = ae^{-bt}$	a, b
modified pore blocking	$J_w = J_\infty + ae^{-bt}$	J_∞ (limiting water flux), a, b

Table 3. Four classical models used in data fitting for the PRO gypsum scaling study.

Highlights

- This work focuses on the elucidation of various underlying mechanisms responsible for the flux reduction in PRO processes.
- Both inner-selective and outer-selective thin film composite (TFC) hollow fiber membranes are employed to examine how the fundamental *internal* factors interact with one another, resulting in various behaviours of *external* performance indexes such as water flux, reverse salt flux, and power density.
- The insights obtained from the stationary conditions are combined with the advanced nucleation theory to elucidate the dynamic scaling process by visualizing how the multiple fundamental factors evolve and interplay with one another in various membrane regimes during the whole scaling process.
- This study may provide useful insights to design more suitable TFC hollow fiber membranes and to operate them with enhanced water flux so that the PRO process may become more promising in the near future.

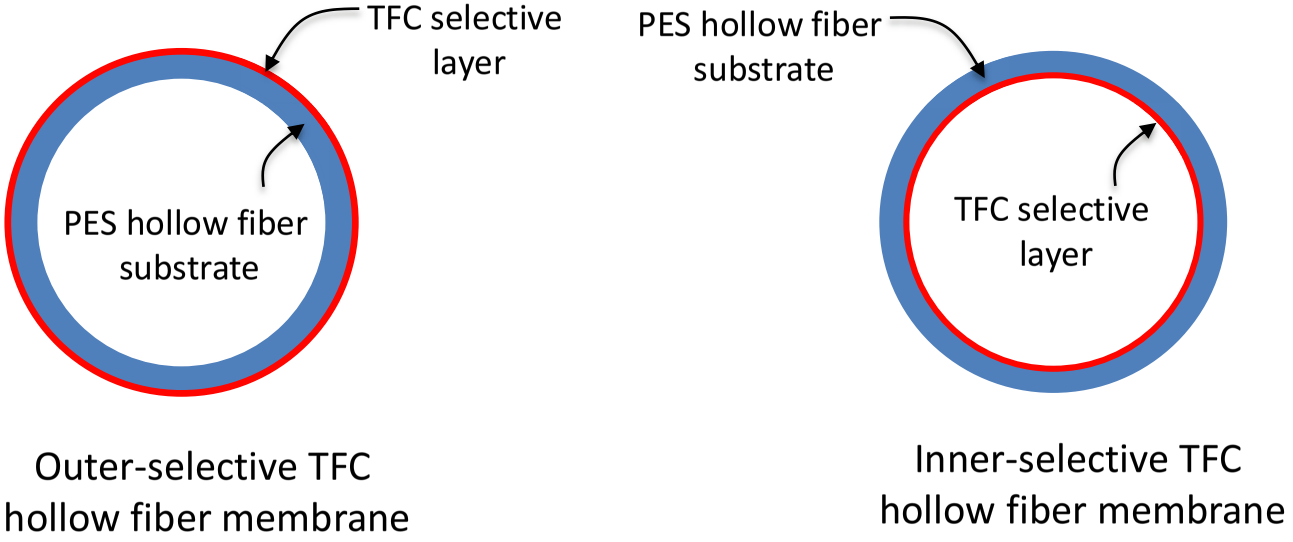

Fig. 1 A schematic illustration of the inner-and outer-selective TFC hollow fiber membranes.

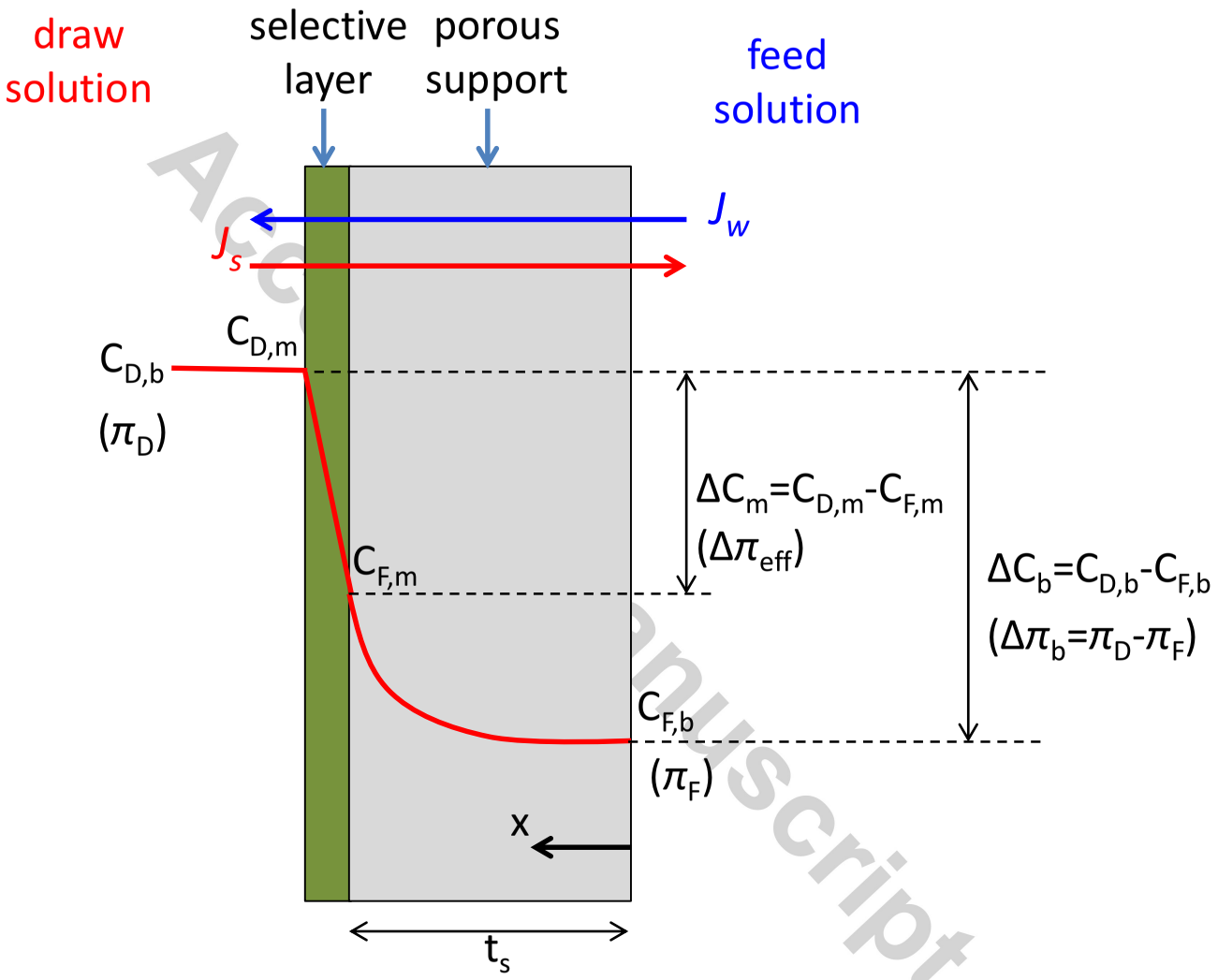

Fig. 2 A schematic diagram of salt concentration across a TFC PRO membrane at steady state. Osmotic pressures corresponding to salt concentrations at different locations are illustrated in the brackets near the concentrations. In this study, the salt concentration on the surface of the selective layer ($C_{D,m}$) is nearly equal to the concentration of the draw solution in the bulk ($C_{D,b}$) due to the negligible external concentration polarization (ECP).

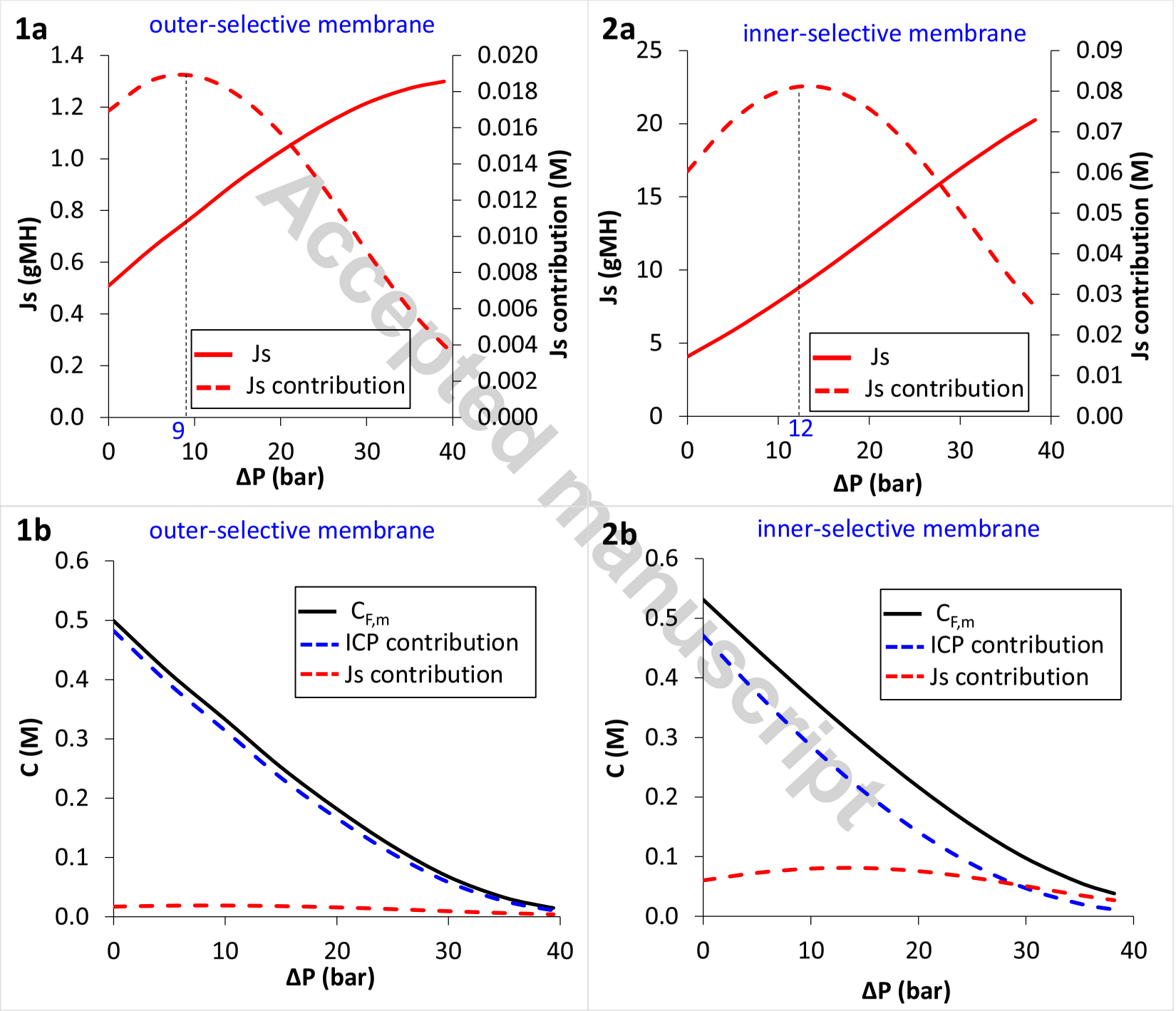

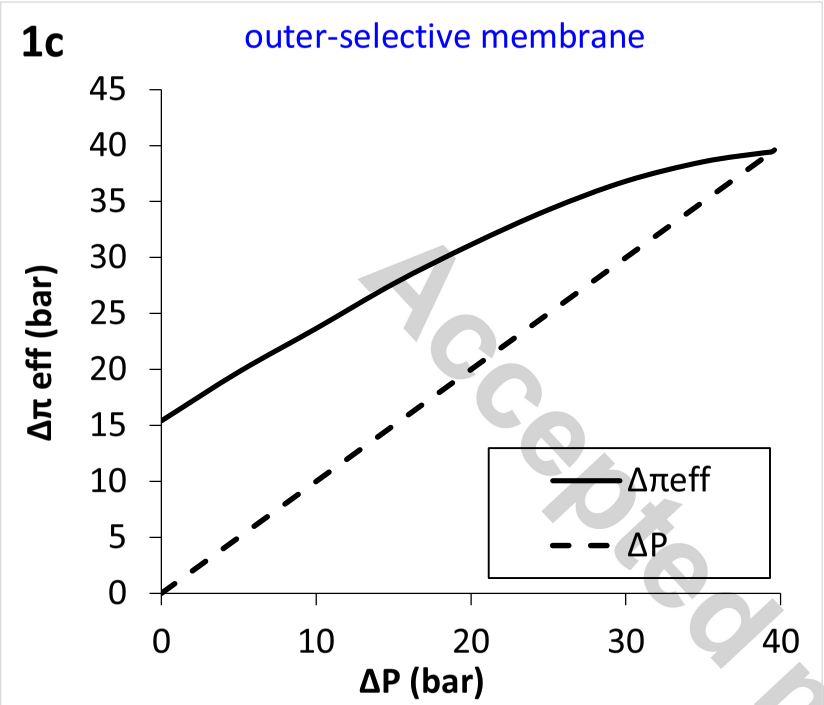

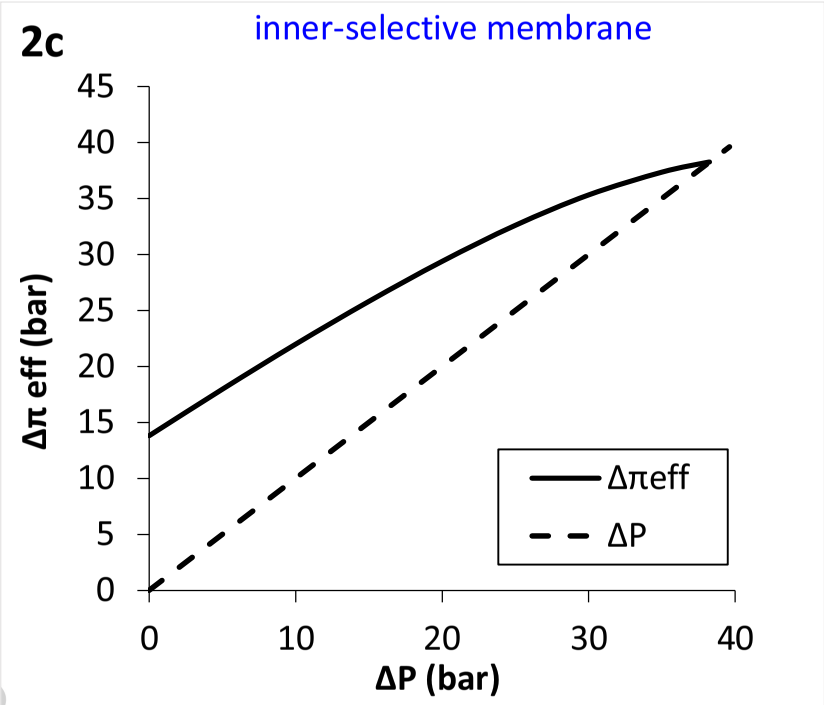

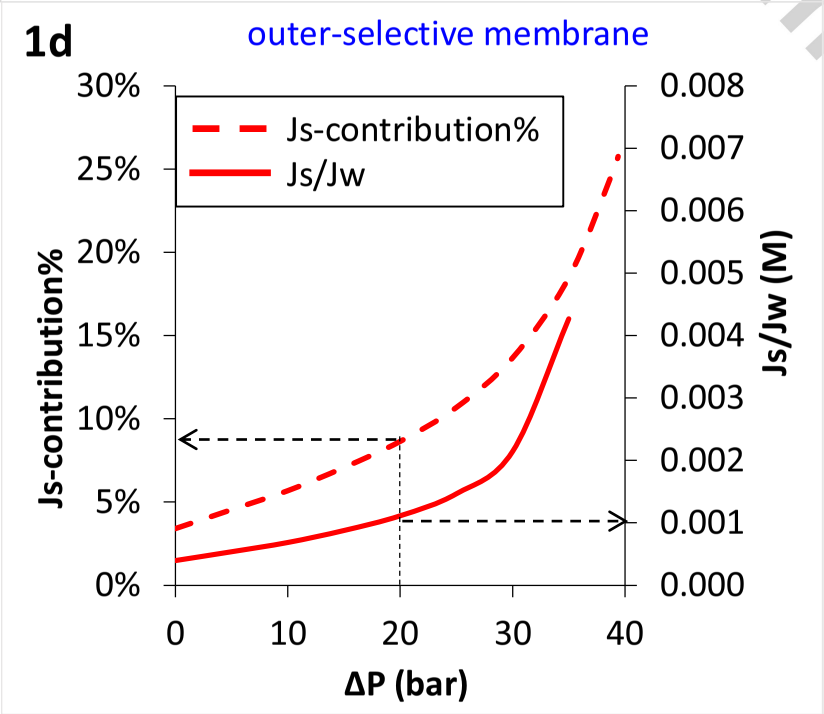

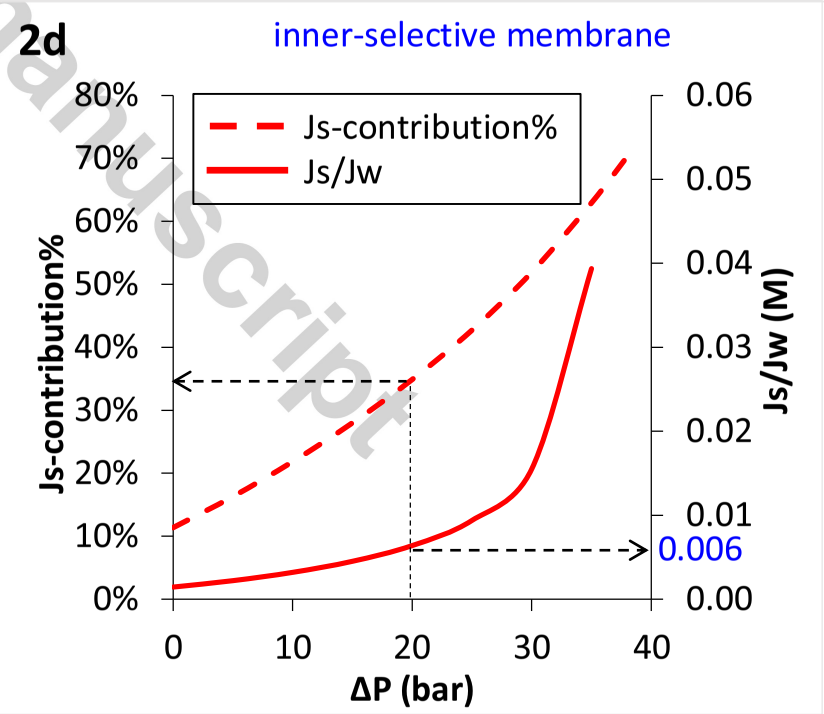

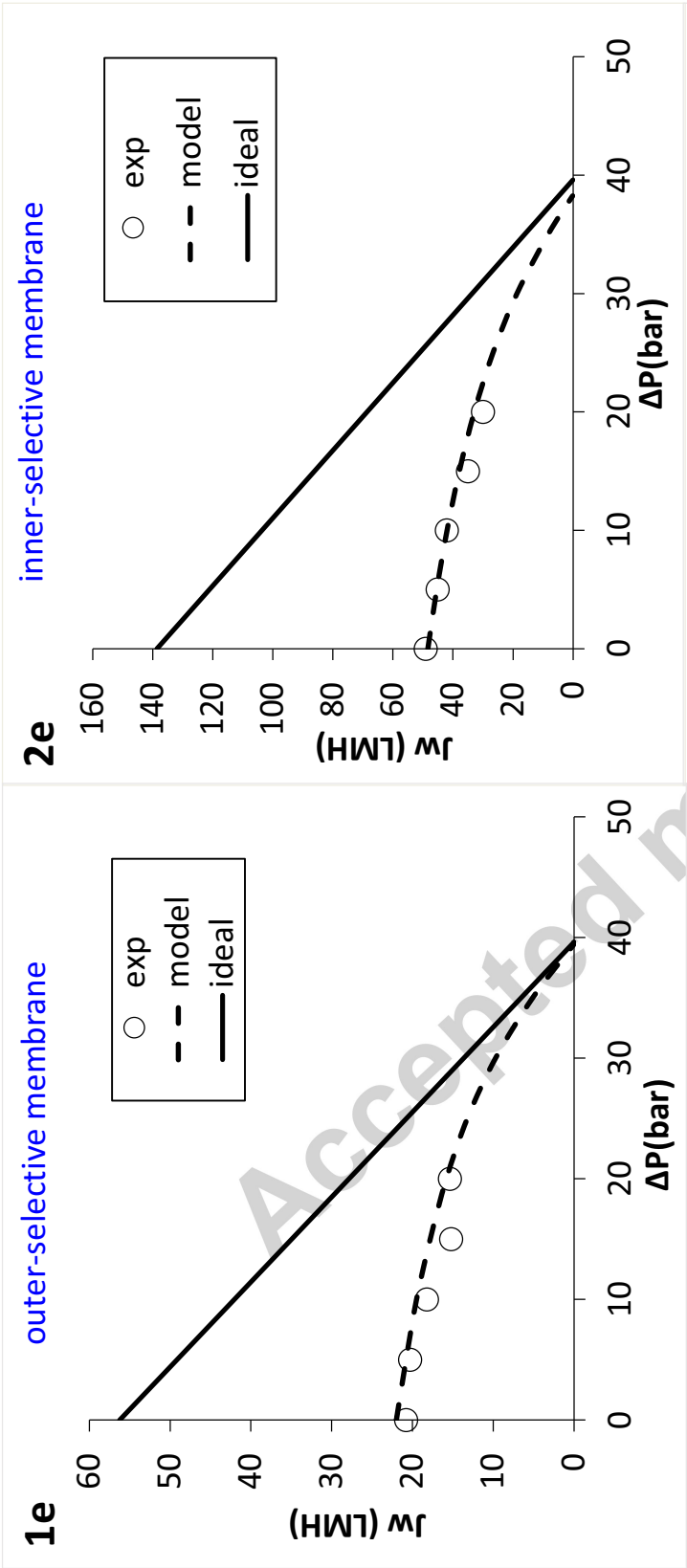

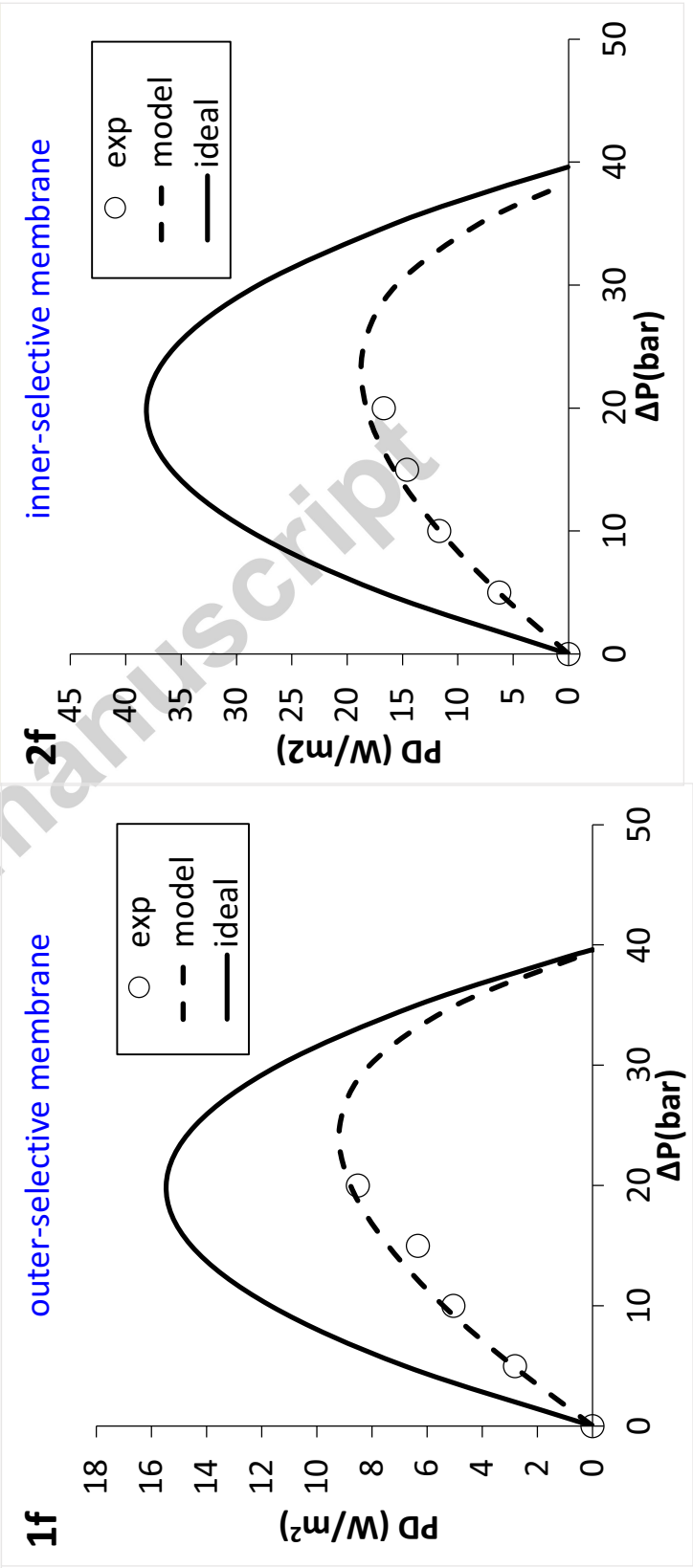

Fig. 3 Various variables in the PRO model as a function of operation pressure (ΔP) under the fixed bulk salinity gradient (draw solution: 0.81 M NaCl vs. feed: 0.011 M NaCl). Series 1a to 1f and 2a to 2f correspond to the outer-selective membrane and the inner-selective membrane, respectively. Ideal: simulation results without considering concentration polarization and reverse salt permeation; model: simulation results with internal concentration polarization (ICP) and reverse salt permeation taken into account; exp: experimental data.

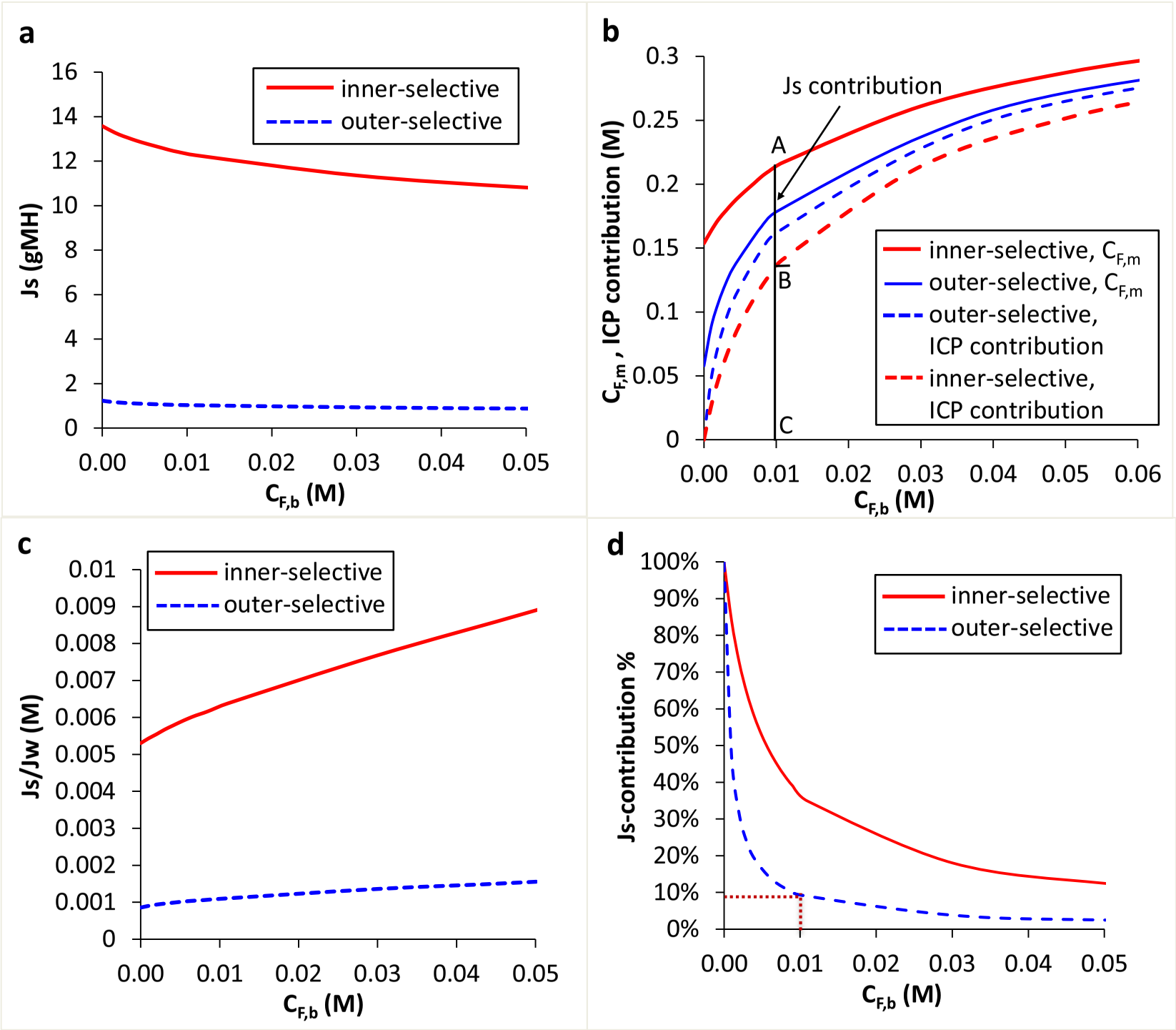

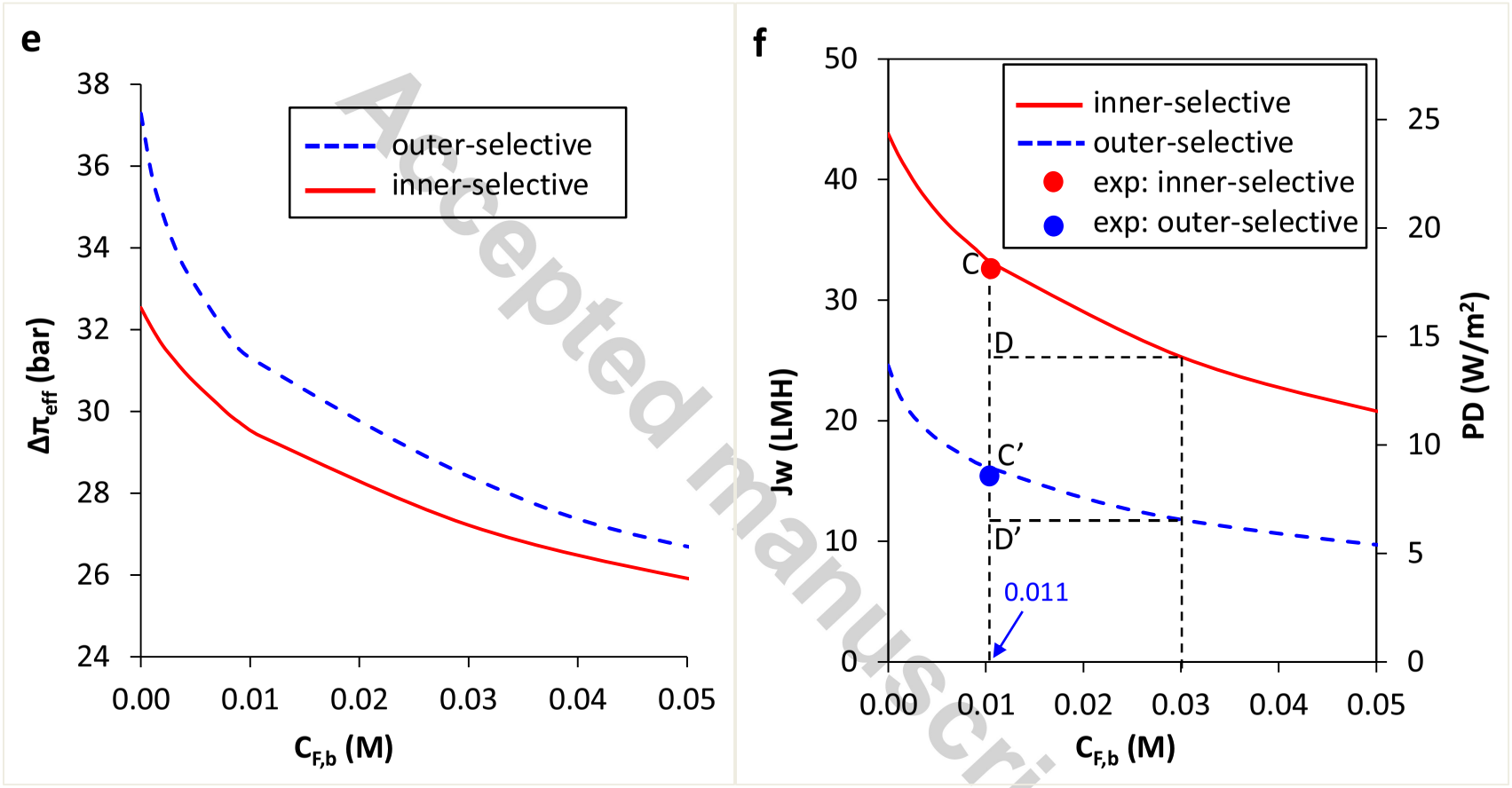

Fig. 4 Comparison of various variables of inner- and outer-selective TFC hollow fiber membranes as a function of feed bulk salinity ($C_{F,b}$). The draw solution has a fixed bulk salinity of 0.81M NaCl and the operation pressure is set at 20 bar. Solid and dashed red lines are the simulation results of the inner-selective membrane; solid and dashed blue lines are the simulaton results of the outer-selective membrane. exp: experimental data.

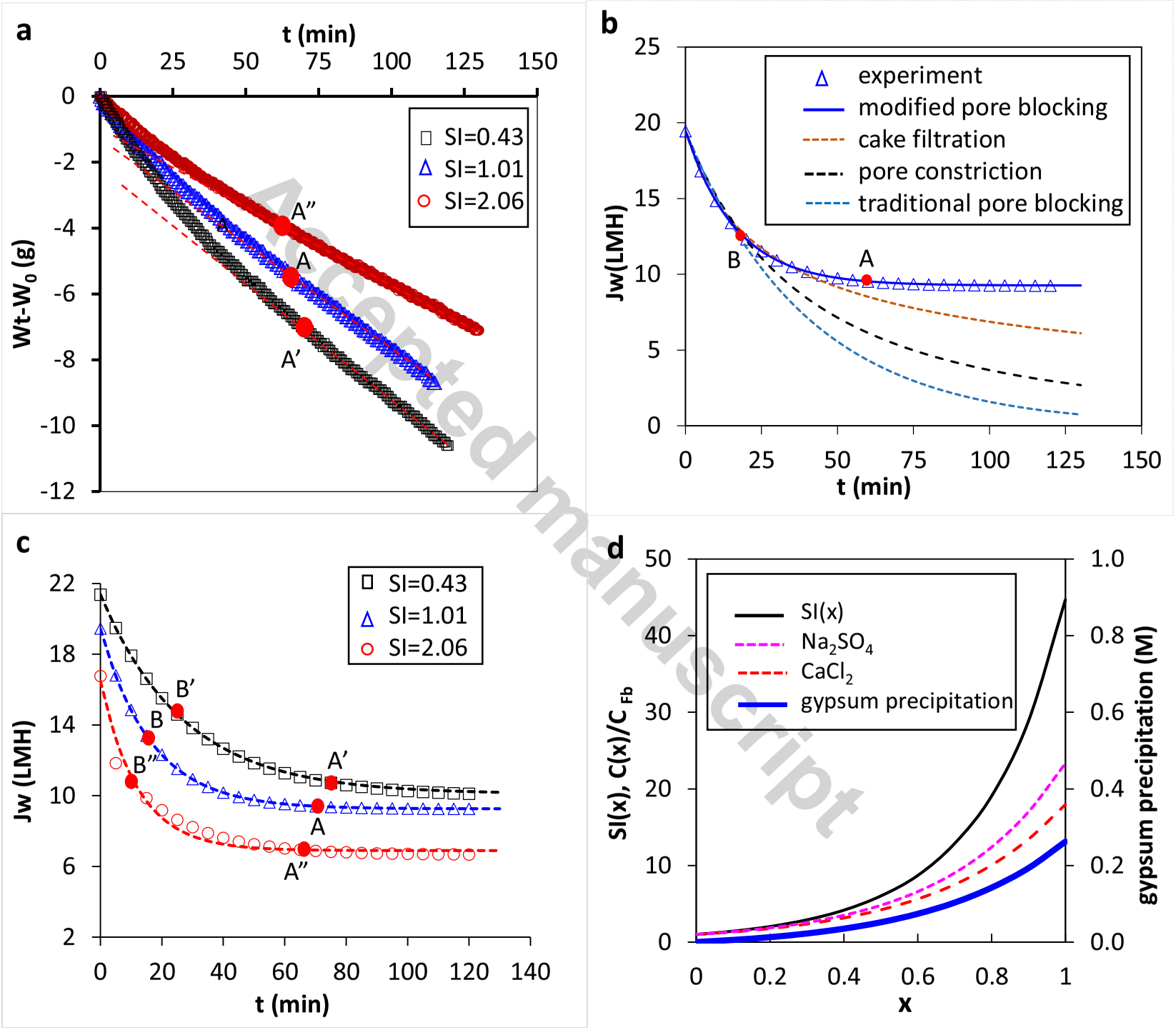

Fig. 5 Investigation of PRO gypsum scaling at a fixed operation pressure (ΔP) of 10 bar. (a) weight loss of the feed as a function of time for different bulk feed saturation indices (SI). W_0 is the initial weight of the feed while Wt is the weight at time t. (b) Data fitting of the flux reduction curve for the bulk feed SI=1.01 with four models. (c) Flux reduction curves for bulk SI=0.43, 1.01, and 2.06. Separate symbols are experimental data. Dotted lines are the fitted curves using the modified pore blocking model. (d) Simulated saturation indices (SI), dimensionless precursor concentrations for $CaCl_2$ and Na_2SO_4 and gypsum precipitation as a function of location inside the membrane porous support. x=0 is the surface of the membrane porous support facing the bulk feed. x=1 represents the interface between the porous support and the selective layer.

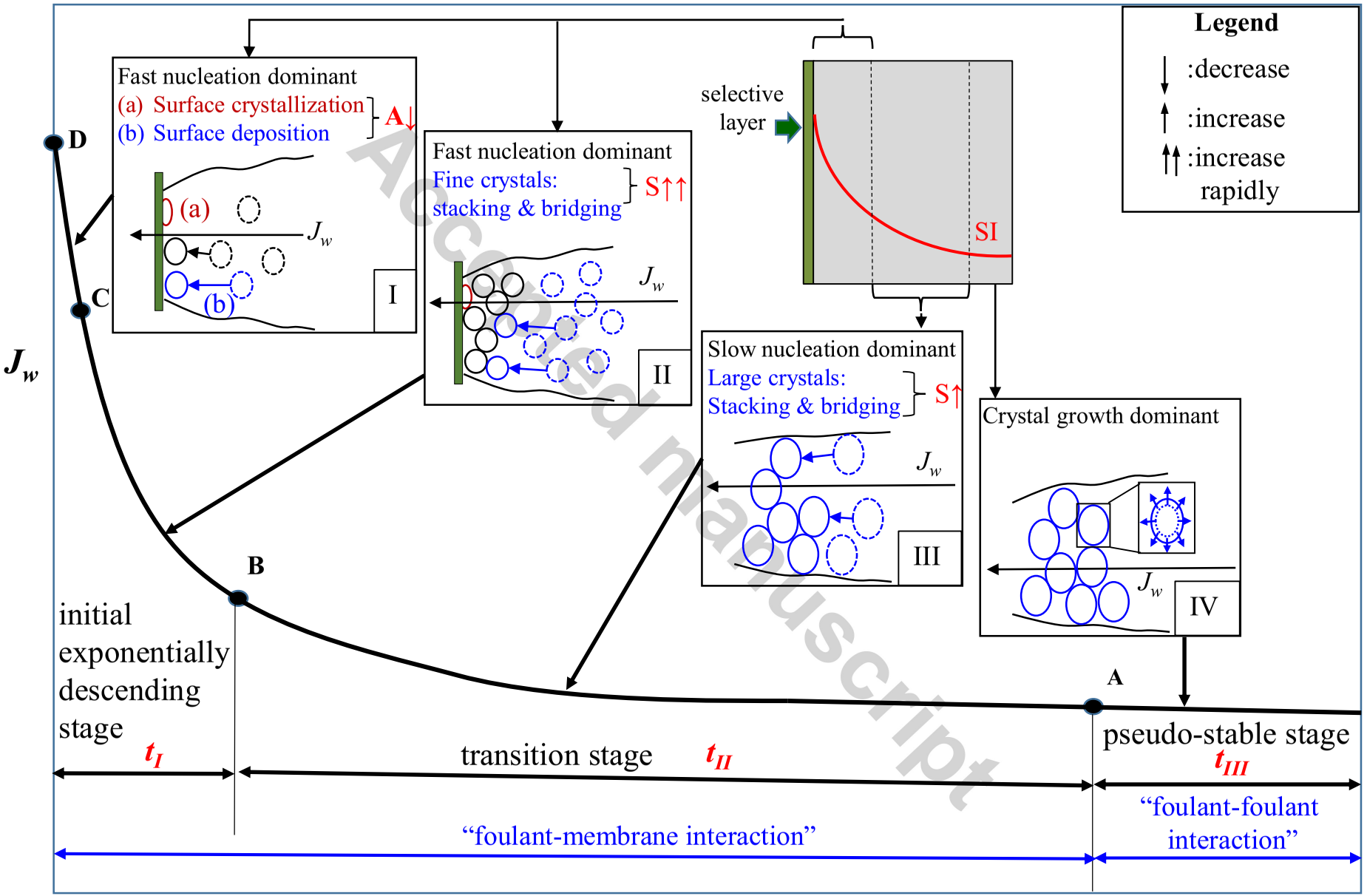

Fig. 6 Schematic presentation illustrating mechanisms of gypsum scaling.

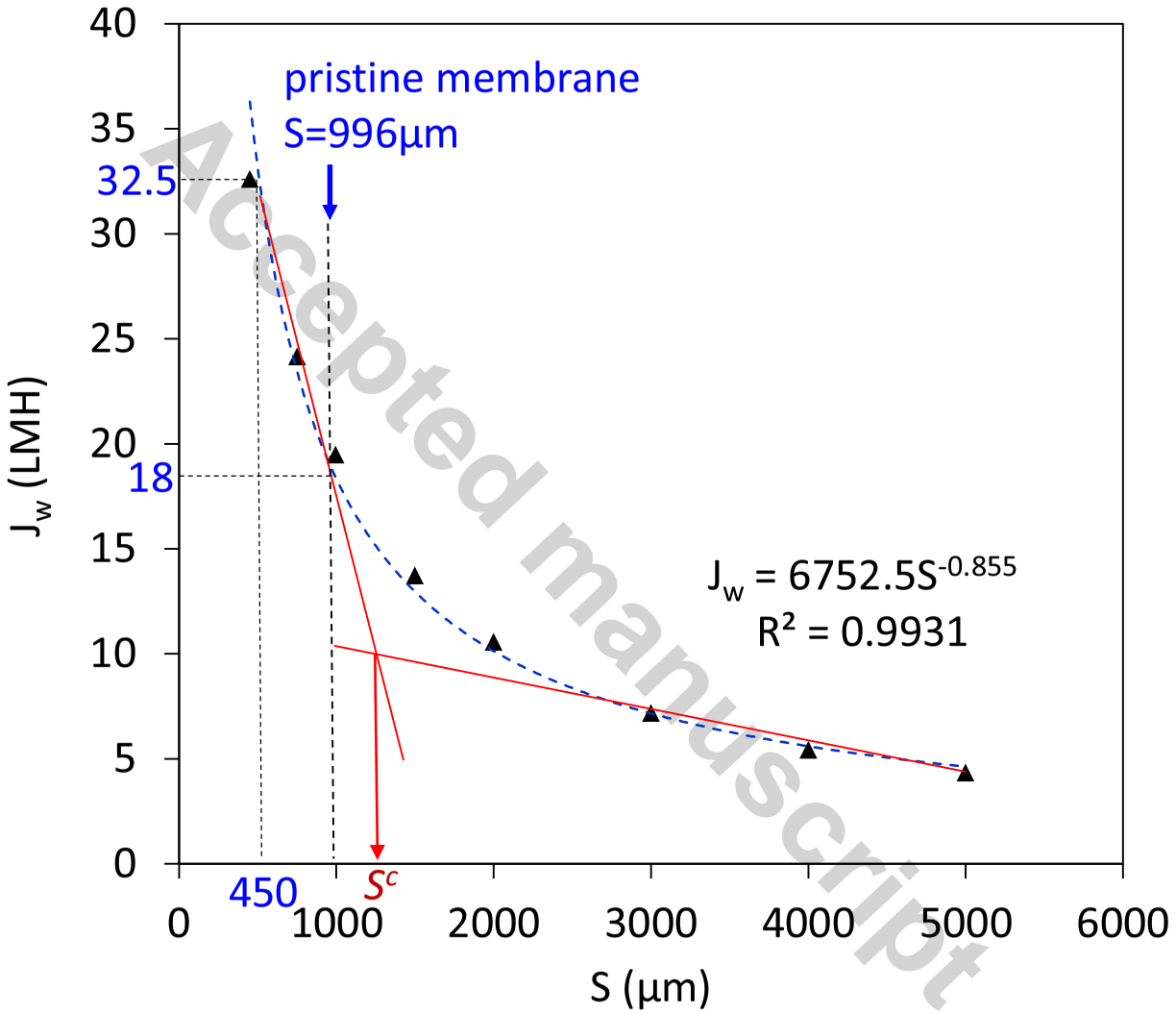

Fig. 7 Water flux as a function of structural parameter for the outer-selective membrane at a fixed operation pressure of 10 bar. Water permeability (A) and salt permeability (B) remain unchanged. The dotted line is the best power fitting.

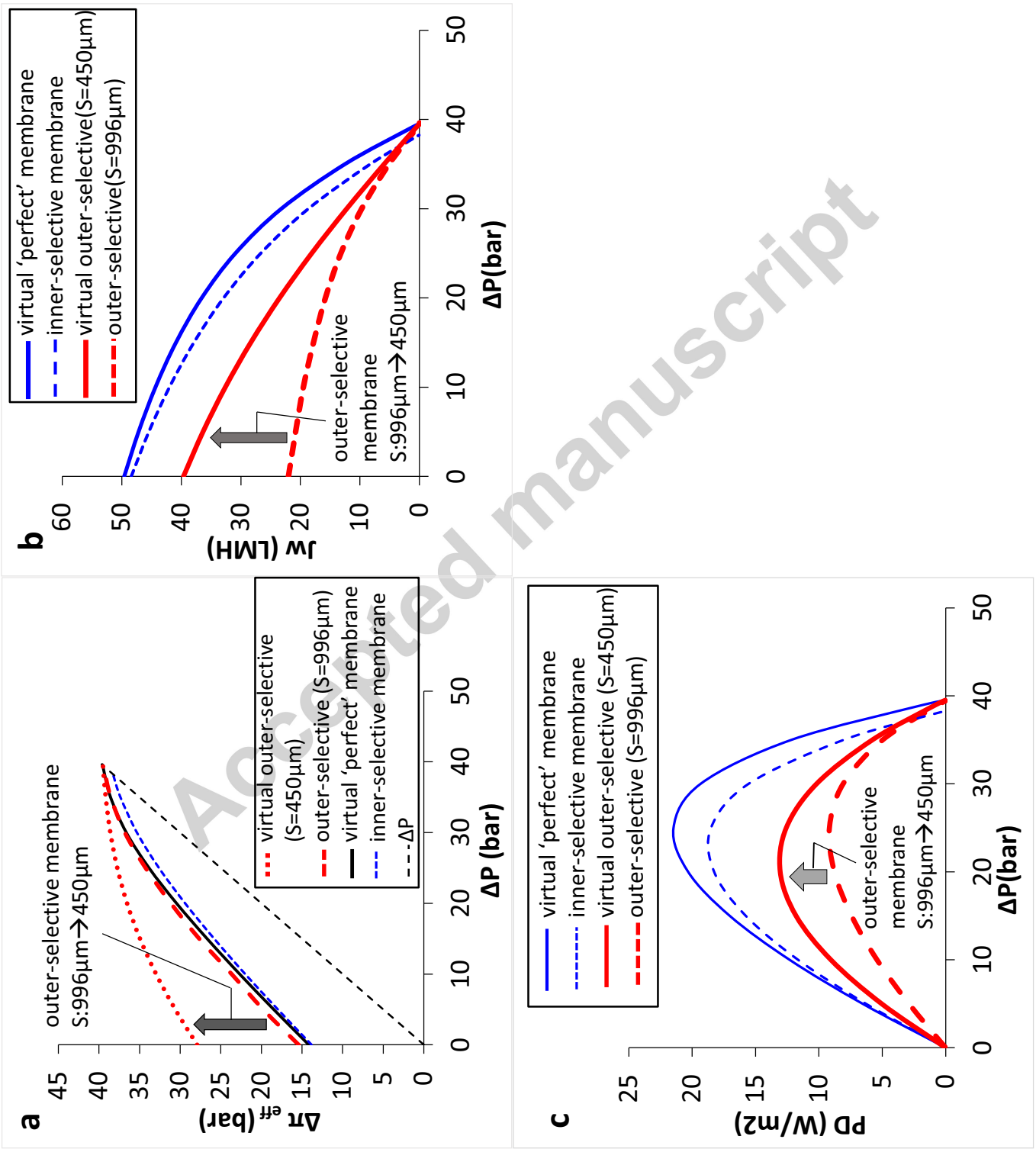

Fig. 8 Effective osmotic driving force ($\Delta\pi_{eff}$), water flux (J_w) and power density (PD) in the PRO model as a function of operation pressure (ΔP) under the fixed bulk salinity gradient (draw solution: 0.81 M NaCl vs. feed: 0.011 M NaCl). The virtual 'perfect' membrane has combined strengths of the inner- and outer-selective membranes (i.e., A=3.5LMH/bar, B=0.028LMH, S=450μm). The virtual outer-selective membrane has a smaller structural parameter (i.e., S=450μm) while A and B values remain unchanged.

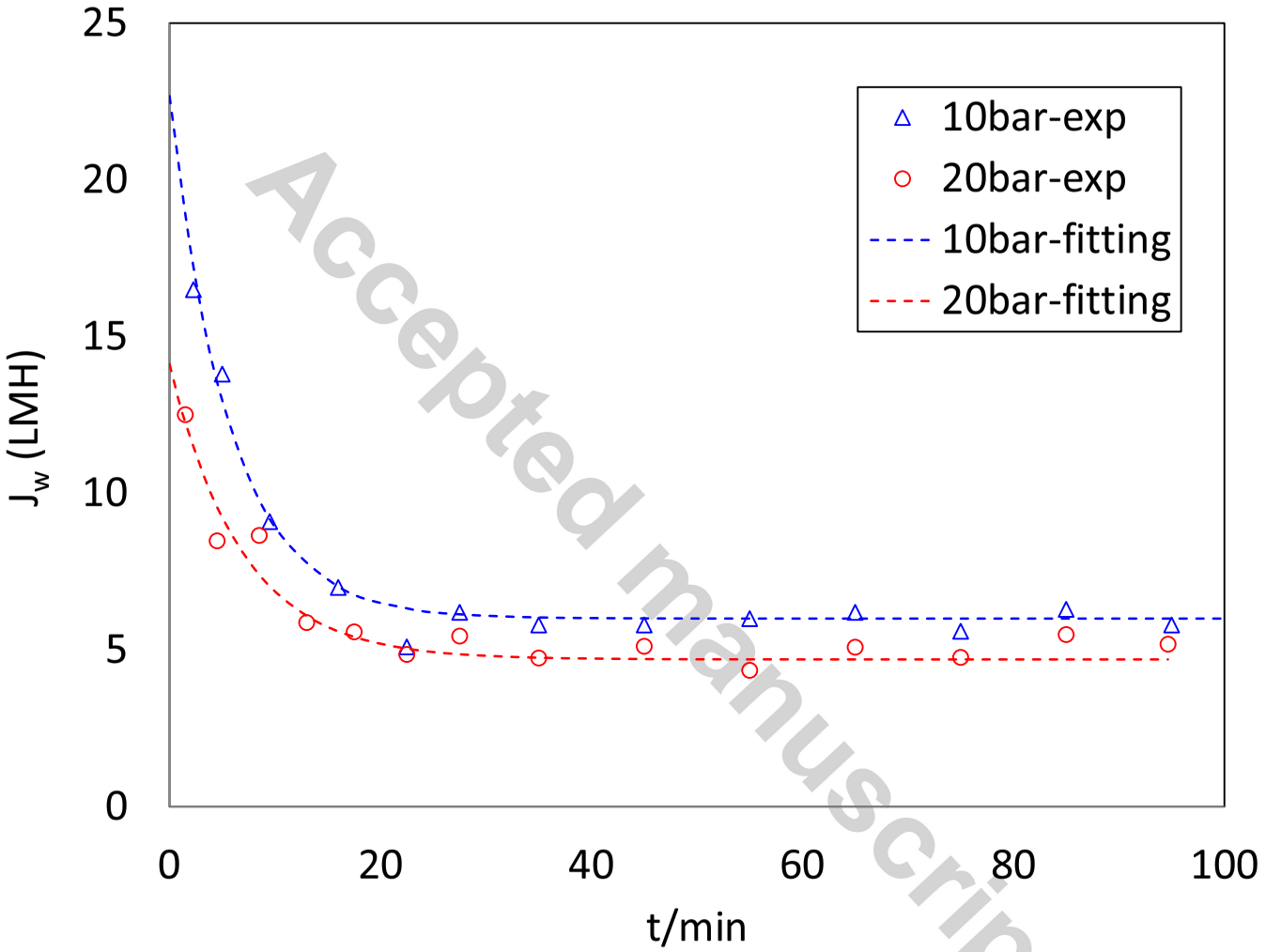

Fig. 9 Water flux as a function of time when 0.81 M NaCl is used as the draw solution and a typical local waste water retentate is used as the feed. Separated symbols are experimental data and dotted lines are the fitting curves using the modified pore blocking model.

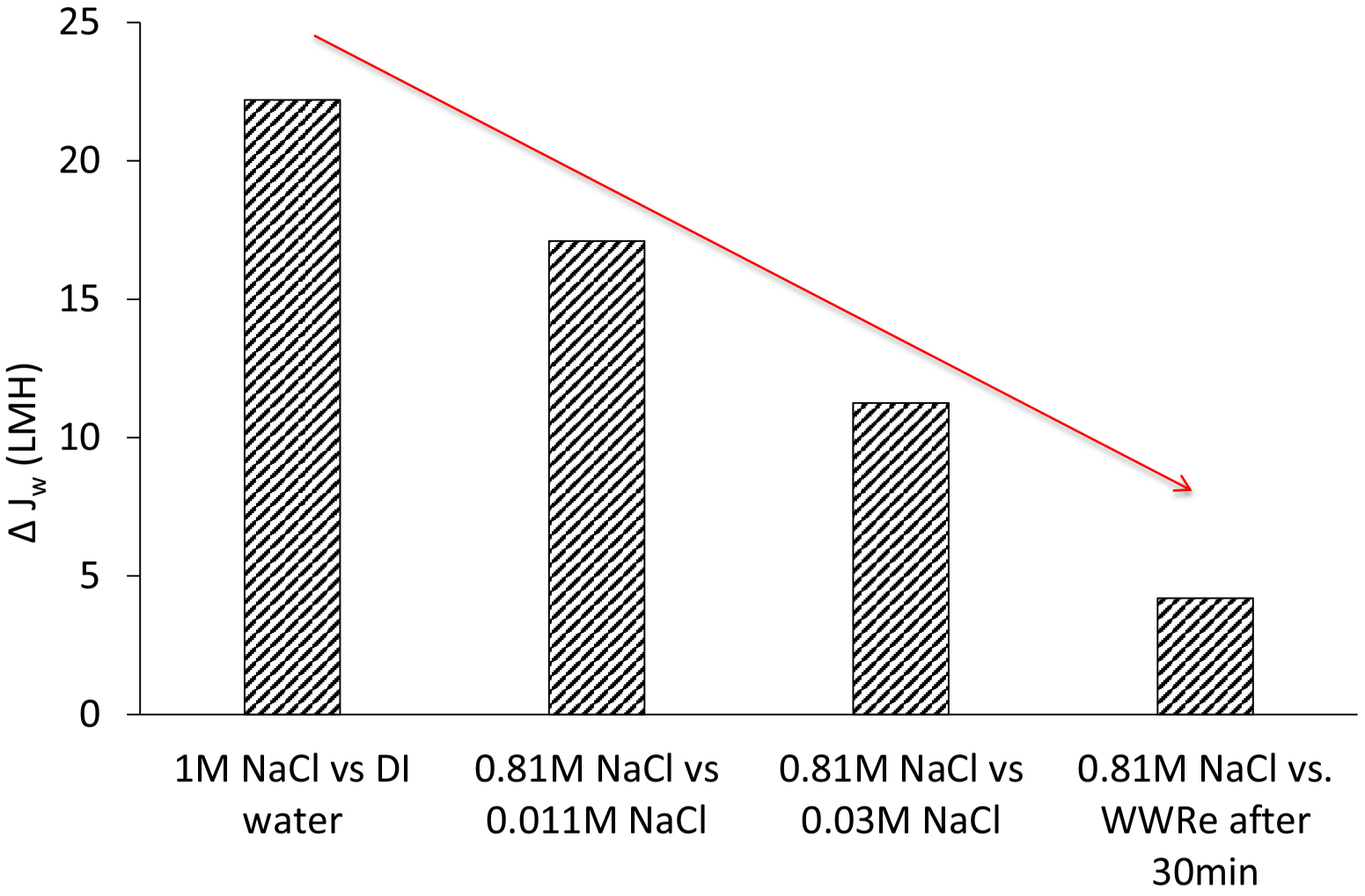

Fig. 10 Water flux differences between inner- and outer-selective hollow fiber membranes at a fixed operation pressure (ΔP) of 20 bar with different feed pairs. The first 3 water flux differences are obtained by simulation, and the last one (i.e., 0.81M NaCl vs WWRe) is from experimental data. WWRe: waste water retentate from a local RO plant using MBR permeate as the feed.

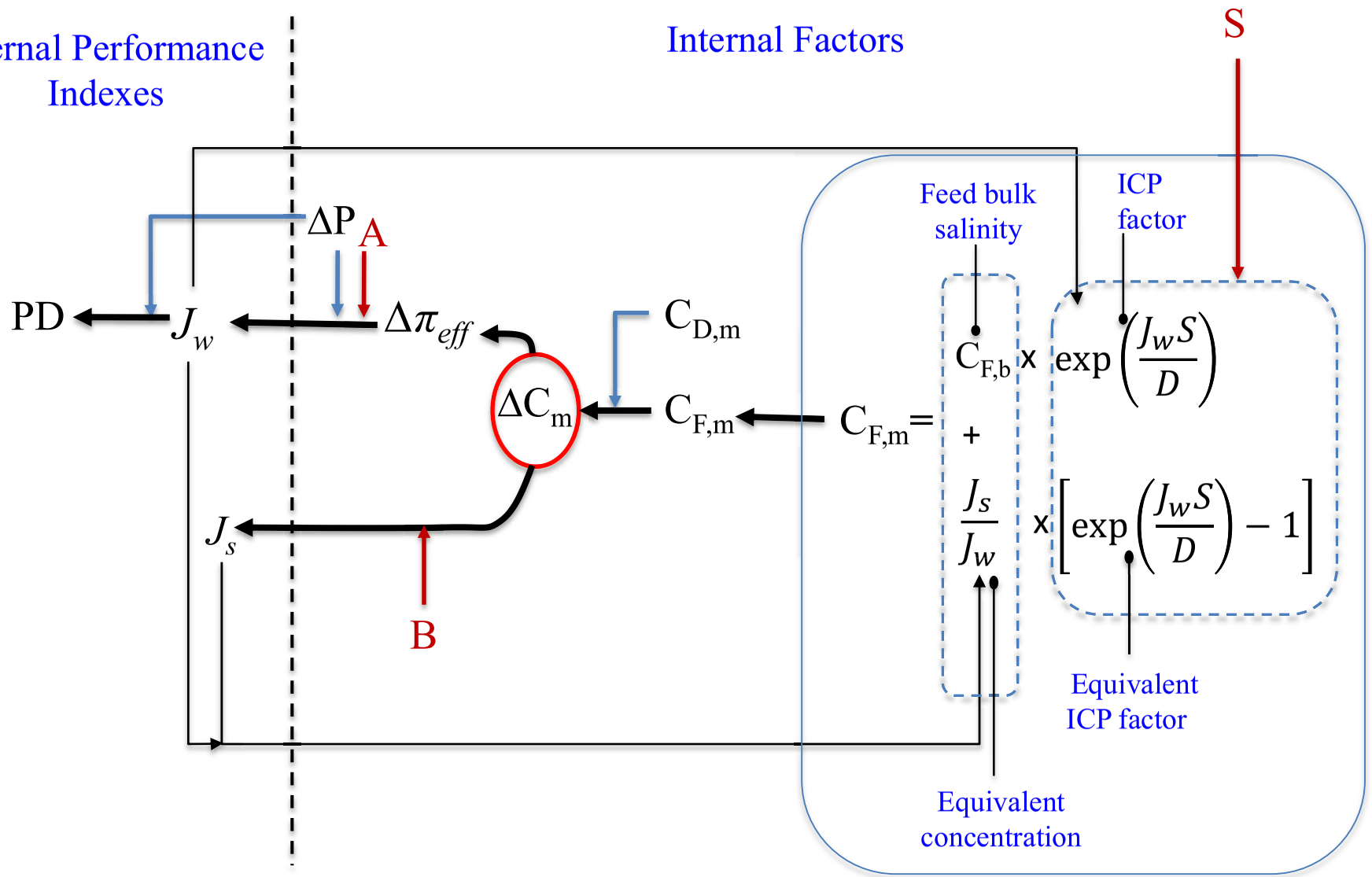

Fig. 11 Schematic system diagram illustrating the relationship between external performance indexes and internal factors. PD is the power density. $\Delta\pi_{eff}$ is the effective osmotic pressure difference across the membrane. ΔC_m is the salinity gradient across the selective layer. $C_{D,m}$ is the surface salinity of the selective layer facing the draw solution. $C_{F,m}$ is the surface salinity of the selective layer facing the feed. $C_{F,b}$ is the bulk salinity of the feed.